LUND UNIVERSITY
MASTER THESIS

Developing a technique for combining light and ultrasound for deep tissue imaging

Author:
Meng Li

Supervisor:
Stefan Kröll

LUND
UNIVERSITY

A thesis submitted in fulfillment of the requirements for the degree of Master in Photonics

Project duration: Sep. 2017- May 2018

LRAP-546

Department of Physics
Atomic Physics Division

Abstract

Biological tissues are strongly light-scattering and absorbing media that limit the depth of optical-based imaging. Even though, optical imaging provides good optical contrast information of biological content that is beneficial for clinical diagnostics application. Ultrasound was used to assist the optical-based imaging technique in overcoming the poor spatial resolution and shallow imaging depth difficulties. Ultrasound can penetrate deep into tissue. When the tissue is illuminated, the ultrasound modulates the light inside the ultrasound focus. The modulated light that shifted by one ultrasound frequency is called the tagged photons. Measure of the tagged photons intensity distribution would provide local light irradiance information in the tissue, and this is the principle of ultrasound optical tomography (UOT). The UOT system can have a spatial resolution as good as the ultrasound focus. The goal of this thesis work is to check the feasibility of UOT at 606 nm. The thesis work was first started with characterizing tissue models with controlled optical properties, homogeneity and macroscopic geometry. Then the performance of an ultrasound scanner was investigated. The UOT experiment was carried out on multiple tissue models with different thicknesses but the same optical properties (μ_s'= 5 cm^{-1}, μ_a = 0.02 cm^{-1}). When the laser energy was 30 nJ (15 mW $\times$ 2 μs), the current UOT system can detect UOT signal for a 40 mm thick tissue model. And it was also capable of performing a 1D line measurement on a 10 mm thick highly scattering medium with an absorbing inclusion in the center, the dimension of the inclusion can be estimated from the UOT measurements.

Acknowledgements

There are so many of you I own my thanks for supporting me through my master thesis work! I would like to express my grandest gratitude to my supervisor Stefan Kröll. Thank you very much for offering me this fascinating project and spending countless hours discussing the project with me, thank you very much for all the efforts you put into supervising me. You are so knowledgeable and kind, thank you very much for always being so concerned and supportive.

I would like to thank Nina Reistad genuinely, thank you very much for sharing your knowledge in medical optics and allowing me using your experimental setup. The UOT experiment cannot be carried out without your help and support. And thank you so much for showing me the ongoing photoacoustic tomography (PAT) measurement in Skånes universitetssjukhus, it was so cool to be able to see the PAT imaging in clinic application in person. I would like to thank Tobias Erlöv and Magnus Cinthio for not only lending me the fancy ultrasound scanner but also spending a lot of hours sharing me the knowledge of ultrasound. Thank you for always being there when I ran into troubles with the scanner.

I would like to thank my friend and colleague Mengqiao Di, thank you very much for your company for the last two years during the lectures, lunch, and lab. And thank you very much for making such an amazing spectral filter to assist the UOT measurement, without your hard work I would not be able to complete the project. I would like to thank my another friend and colleague Alexander Bengtsson, I appreciate all the time you spent in the lab and your assist, and thanks for your cookies too.

I would like to thank all my 'co-supervisors' from the Quantum Information Group, you all are so kind and supportive, thank you for making me always feel welcomed. I would like to specific thanks Chunyan Shi, Sebastian Horvath, Adam Kinos and Qian Li. Thank you all so much for using your 'magic power' bring the 606 nm laser from 'dying' to 'alive', thank you very much for spending your free time to help me. And thanks Sebastian again for 'resurrected' my photomultiplier tube as well, that literately saved my project. Thank you very much David Hill for proofing reading my thesis and your comments, they are of great help.

I would like to thank my friends for always being there for me. Especially thanks Vidar Flodgren for proofreading my popular science. Now it is yours and Tim's turn to choose your adventure book, good luck!

Personally, I would like to thank my family my love Karl Bastos. You are always so patient and so kind. Thank you for your full-time support and care and love.

Popular Science

The discovery of X-rays was the key to developing medical imaging methods. Since then, medical imaging techniques have advanced to the point where it can provide real-time, 2D or 3D, visual representations of the internal structures of a human body. The three most commonly used techniques are MRI, CT, and PET scans, all with their advantages and disadvantages. The MRI uses a strong magnetic field to reconstruct an image from resonating atoms, but this means that patients with metal implants, like pacemakers, cannot perform an MRI scan. Patients can also be allergic to the radiotracers used in the PET scan, and exposure to the X-rays during a CT-scan carries a risk of cancer. Thus, the world is still looking for other imaging techniques that can overcome those limitations.

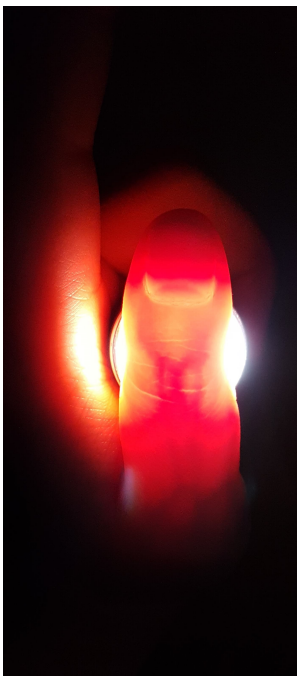

Medical imaging shares the same basis as photography. If using a regular camera, to be able to take a picture of an object, you first need to be able to see it. In a pitch-black room, you would not be able to image the object without using the flash on the camera, there needs to be enough light to register an image on the camera sensors. If you enable the flash mode on your camera and block the flash with your hand, you should notice that your hand glows red when the flash is on. The reason your hand glows red color is due to the absorption of the tissue is wavelength dependent. For human tissue, more blue light is absorbed compare to red light. Even though light travels through tissue in such a way that it appears that light fills the inside, but it does not allow an observer from outside to see any structure within it. This is because light scatters in all directions multiple times while inside the tissue, there is no way we can directly trace back where the light we observed came from. If all the light particles, called photons, that passed through a certain region inside the tissue were labeled, even if they were scattered away afterward, we can still determine the origin of these labeled photons. That is the fundamental principle of developing the imaging technique called ultrasound optical tomography (UOT). Focused ultrasound and light are simultaneously applied to the tissue. Photons inside the ultrasound focus are tagged; the intensity of tagged photons is dependent on the encountered biological contents optical properties. An UOT tissue image can be acquired by moving the ultrasound focus while recording the tagged photons intensity changes.

Contents

List of Abbreviations

AOM	**A**cousto-**O**ptic **M**odulator
AOTF	**A**cousto-**O**ptic **T**unable **F**ilter
APD	**A**valanche **P**hotodiode **D**etector
CFD	**C**onstant **F**raction **D**iscriminator
CW	**C**ontinuous **W**ave
FWHM	**F**ull **W**idth **H**alf **M**aximum
Hb	Deoxyhemoglobin
HbO_2	Oxyhemoglobin
IRF	**I**nstrument **R**esponse **F**unction
LCF	**L**iquid **C**ore **F**iber
MRI	**M**agnetic **R**esonance **I**maging
NIR	**N**ear **I**nfrared **R**ed
PAT	**P**hoto**A**coustic **T**omography
PET	**P**ositron **E**mission **T**omography
PMT	**P**hoto**M**ultiplier **T**ube
PTOF	**P**hoton **T**ime **O**f **F**light
PW	**P**ulsed **W**ave Doppler
RTE	**R**adiative **T**ransport **E**quation
TCSPC	**T**ime **C**orrelated **S**ingle **P**hoton **C**ounting
UOT	**U**ltrasound **O**ptical **T**omography
US	**U**ltra**S**ound
WMC	**W**hite **M**onte **C**arlo

Chapter 1

Introduction

1.1 Motivation

In the field of healthcare, there have been significant developments in medical imaging systems in the past century. They can create visual representations of the human internal structures such as bones or organs. They have made a significant impact on assisting clinical analysis, medical therapy, and early cancer detection. The top three most commonly used medical imaging techniques are magnetic resonance imaging (MRI), computerized X-ray tomography (CT) and positron emission tomography (PET). However, those imaging techniques are not only expensive and cumbersome but also associated with potential risks. Patients with metal implants/allergies have limited choices of deep tissue imaging systems. Moreover, for pregnant patients, they cannot use either of those three imaging techniques because exposure to radiology-based imaging techniques or strong magnetic forces poses a significant threat to the health of the fetus. Because of the drawbacks of these techniques, it is desirable to develop a new, low cost, deep tissue imaging technique, one that can be used on anyone without any medical constraints.

Optical-based imaging is gaining traction in the medical imaging field. This technique has the potential to provide tissue spatial and spectral information based on optical contrast. From the visual perspective, light can only interact with matter in two ways; it can either be absorbed or scattered. Both optical and PET scan techniques suffer from the lack of contrast and specificity due to the high scattering and absorption within the biological tissue. To overcome those challenges, PET scan uses radiocontrast agents, whereas optical imaging uses biomarkers to target specific biological content to enhance the correlated contrast. Given the high specificity of a biomarker, it can be used as a drug carrier [1]. Nevertheless, the fluorescence of the biomarker might overlap with the autofluorescence of the biological tissue, e.g., phenylalanine and tyrosine both have autofluorescence feature [2], it becomes challenging to separate the fluorescence signal from the autofluorescence background.

An example of successfully developed tissue optic techniques is pulse oximetry. Pulse oximetry is used to measure blood oxygen saturation; it sends out two wavelengths through a fingertip/earlobe (thin section of the body) to a photodetector.

Different variants of tissues exhibit different optical properties. For example, oxygenated and deoxygenated hemoglobin would absorb different amounts of light at the same wavelength. Tumorous tissues have different biological compositions from the surrounding healthy tissue, which means their optical properties are significantly different. If the optical-based imaging is capable of distinguishing different biological contents based on collected optical information, it has the potential to perform deep tissue imaging based on optical contrast. However, the light that comes out of the tissue encounters multiple scattering and absorption events, and there is no way of reconstructing where and when the light underwent changes inside the tissue. To enhance the correlated contrast for optical imaging technique without invasiveness (the injection of biomarker), it requires the assistance of other imaging technique. One idea involves the ultrasound imaging technique. The ultrasound can penetrate deep into the tissue with a relatively high mechanical contrast remain.

1.2 Aim

The aim of this thesis is developing an ultrasound optical tomography (UOT) technique, seek to keep the advantages of both optical and ultrasound imaging methods and overcome both their limitations. The principle of UOT is tagging the photons inside the medium with focused ultrasound, the ultrasound modulates the medium refractive index and turns it into a phase and amplitude grating. Light diffracted on the grating is frequency shifted by one or multiples of the ultrasound frequency. The light irradiance in the medium can be mapped out by monitoring the tagged photons' intensity while moving the ultrasound focus. The UOT should be able to penetrate deep enough to reach the heart or brain with sufficient contrast-to-noise ratio to measure the blood oxygen saturation [3]. UOT has the potential to acquire images of the interior aspect of the body in a much shorter time than MRI and CT. Meanwhile, UOT does not require radiotracers (meaning the hospital does not need to have a particle accelerator like a cyclotron) nor operate in a strong magnetic field environment (MRI requires superconducting magnets). In an ideal situation, the patient can frequently have an early stroke or tumor/cancer health check before symptoms appear, offering patients a higher survival rate compared to the late-stage diagnose.

Chapter 2

Theoretical Background

2.1 Light-tissue interactions, scattering and absorption

When light interacts with biological tissue, due to the higher refractive index of the tissue medium, Fresnel reflection will happen at the interface, while the rest of the light would penetrate the tissue. As shown in figure 2.1, the light beam disperses and disappears as the light penetrates deeper. Heat can be generated when medium absorbs the light. Once the medium cools down, the relaxation of the medium would generate acoustic waves. There are also special materials that can cause autofluorescence or fluorescence under specific environmental conditions. Scattering (quantified by μ_s) and absorption (quantified by μ_a) of the medium are the most responsible properties for the redistribution of light.

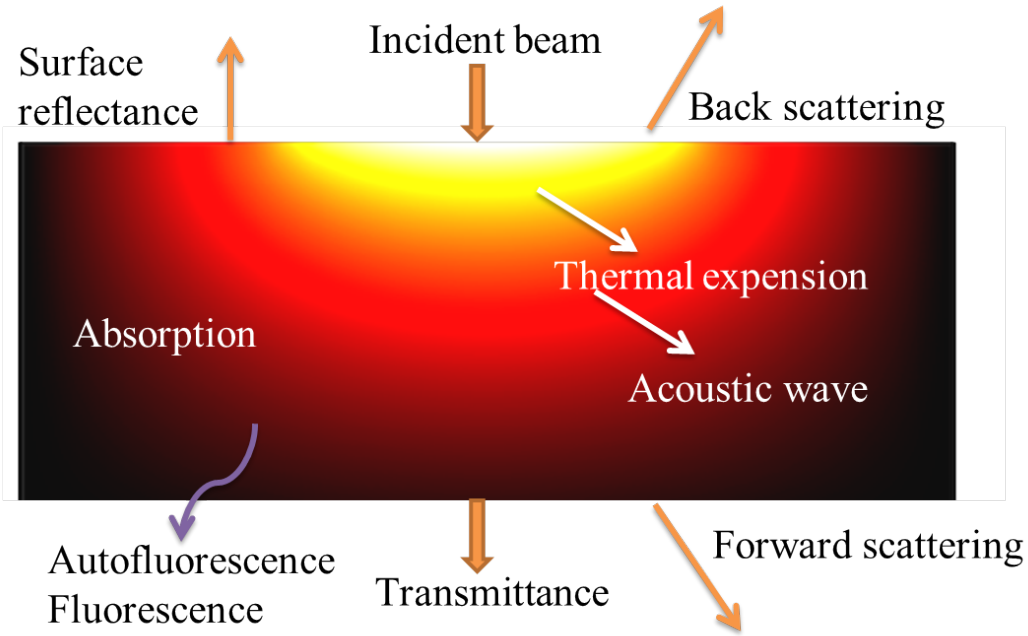

FIGURE 2.1: Multiple events are involved in a light-tissue interaction, light is redistributed based on the optical properties of the medium.

2.1.1 Scattering coefficient

Biological tissue is a highly scattering medium. Each particle inside the tissue is modeled as a homogeneous spherical structure with high refractive index[4] to simplify the simulation and calculation. The scattering coefficient μ_s is defined as the probability per unit length a photon scatters, and it is characterized by a scattering phase function. Few parameters are involved in the phase function to describe a scattering process: θ is the scattering angle in the scattering plane (angle between z-axis and $\vec{S_1}$), and φ is the scattering angle in the x-y plane (angle between x-axis and $\vec{E}_{\parallel i}$), see figure 2.2. The phase function is usually denoted as $p(\theta, \varphi)$, p represents the probability density function for the process where a scattered photon change its trajectory.

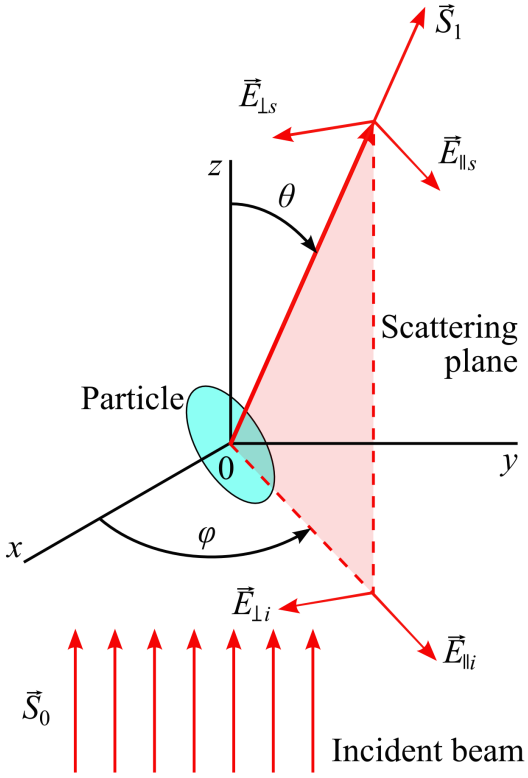

FIGURE 2.2: Geometry illustration of the scattering phase function, image cited from [5]. $\vec{S_0}$ is the incident beam direction which is parallel to the z-axis, and $\vec{S_1}$ is the scattered light direction. On the scattering plane, the two orthogonal polarization components of the scattering lights are presented as vectors $\vec{E}_{\parallel s}$ and $\vec{E}_{\perp s}$, and their projections on the x-y plane are presented as vectors $\vec{E}_{\parallel i}$ and $\vec{E}_{\perp i}$.

The phase function can be simplified and rewritten as $p(\theta)$ when the scattering is symmetric relative to the incident beam, and the phase function is then only dependent on the scattering angle θ. In the figure above, the trajectory of the scattered photon in the z-axis is presented as $cos(\theta)$. There are two scattering types. Rayleigh

scattering happens when the scattering particle size is way smaller than the incoming wavelength, such scattering event is highly wavelength dependent and mostly isotropic. Mie scattering happens when the particle size is larger than the incident wavelength, it is no longer isotropic, and it is mostly in the forward direction (close to the incident beam direction). Mie scattering dominates the light-tissue interaction [4]. The averaged scattering direction is denoted by symbol g, and it is called the anisotropy factor:

$$g =< \cos\theta >= \int_0^{\pi} p(\theta)\cos\theta \cdot 2\pi \sin\theta d\theta. \tag{2.1}$$

g factor is only used in medical optics to describe the angular distribution of scattered light. For an isotropic Rayleigh scattering, the g factor equals 0, and the scattering events are identically distributed in all directions. When the g value varies from -1 to 1, it represents a Mie scattering event. When g equals 1 the particle scatters forward, and when g equals -1 the particle scatters backward. Combining the g factor and μ_s, the reduced scattering coefficient μ_s' can be quantified:

$$\mu_s' = \mu_s(1-g). \tag{2.2}$$

Reduced scattering coefficient represents the diffusion of a photon within the medium where every step is isotropic scattering. When g equals 1, reduced scattering coefficient becomes 0, meaning the incident photon remains its initial direction, there is not scattering event and no losses of information.

During this thesis work, Intralipid 20% from Fresenius Kabi AB was used as a scatterer. Intralipid is also known as lipid emulsion, and it is a medical product that consists of small droplets of fat within the water. Mixture a small percent of intralipid with water would form a highly scattering suspension. Intralipid uniformity was examined by Di Ninni et al[6], the batch to batch variation is 2% for intralipid's reduced scattering coefficient, and its absorption coefficient is minimal and can be treated as equal to the one of water. Since Intralipid is a diffusive reference standard for optical phantoms, it has a known scattering coefficient. René Michels et al. [7] calculated the reduced scattering coefficient for intralipid 20% by fitting to the Mie theory from 400 nm to 900 nm,

$$\mu_s'(\lambda) = y_0 + a\cdot\lambda + b\cdot\lambda^2 \qquad [\mathrm{mm}^{-1}/(\mathrm{ml/l})], \tag{2.3}$$

where the wavelength λ is in nanometers, other parameters y_0 = 8.261E+1, a = -1.288E-1, and b = 6.093E-5 [7], the unit of μ_s' is interpreted as mm^{-1} per ml intralipid 20% per l of total diluted suspension .

2.1.2 Absorption coefficient

The absorption coefficient is defined as the probability of a photon be absorbed when it propagates a unit length inside the medium, and it is denoted as μ_a with unit [cm^{-1}]. The light transforms into multiple different forms of energy, such as heat, acoustic waves or fluorescence. The major absorbers within the biological medium are blood and melanin[8]. Lipid and water show some absorption in the visible light region. But in comparison, they are much weaker than blood. Water becomes a strong absorber in the NIR region.

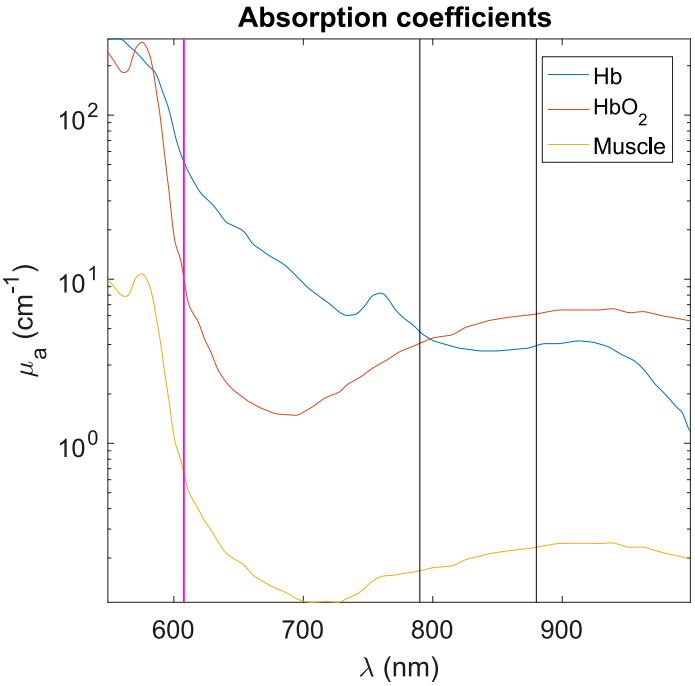

FIGURE 2.3: Absorption spectra for oxy- and deoxyhemoglobin in 100% blood [3], the pink vertical line indicates the wavelength 606 nm, where the rare-earth-ion filter is available during this thesis work.

The hemoglobin protein can be found inside the red blood cells, whose role is transporting oxygen from the lungs to the body cells then return carbon dioxide to the lungs. A hemoglobin with oxygen is termed oxyhemoglobin, $\mathbf{HbO_2}$, when it is without oxygen it is termed deoxyhemoglobin, **Hb**. The oxygen saturation $\mathbf{SO_2}$ is determined by both **Hb** and $\mathbf{HbO_2}$ concentrations:

$$SO_2 = \frac{[HbO_2]}{[HbO_2] + [Hb]}. \tag{2.4}$$

Hemoglobin with and without oxygen present different optical properties. Absorption curves for oxy- and deoxyhemoglobin are present in figure 2.3 in logarithmic scale, which is cited from Walther et al. publication[3]. The muscle curve within

the figure assumes a normal muscle tissue containing 4% of blood and 85% oxygen saturation.

Talens Indian ink purchased from Svenskt Konstnärscentrum was used as the absorber. However, unlike intralipid, ink does not have a controlled production condition, its absorption coefficient varies between brands and batches. Thus, the absorption coefficient of our Indian ink will be measured and discussed in following chapters.

2.2 Light propagation within the tissue

The previous section discussed scattering and absorption from the view of a single photon. However, after light entered tissue, the photons experience multiple scattering and absorption events, which make optical-based imaging in deep tissue challenging. After several random scattering and absorption interactions, light information such as polarization or phase is lost for diffused photons, and it becomes very challenging to retrace the photons trajectories within the medium.

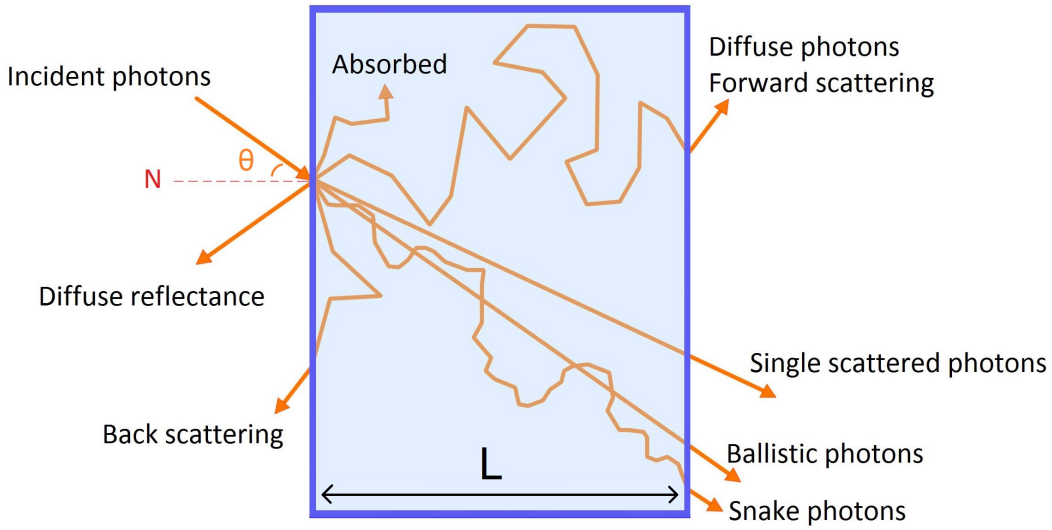

FIGURE 2.4: A schematic of multiple types of scattering events in a turbid medium.

The light propagation regimes are shown in figure 2.4. Assume collimated beam incidents on a scattering medium with an angle θ. Photons that travel straight through the medium without experiencing any scattering event are called ballistic photons, while photons that are scattered but remain in almost the same direction with few degrees of coherence are called snake photons. Light undergoes reflection, refraction, and absorption, but most photons will be diffused in the back and mostly forward directions. Photon time of flight can be calculated for either ballistic or diffused photons, and it is defined as the time required for a photon to travel through

a distance L inside a turbid medium[9] :

$$\text{TOF} = \frac{\frac{L}{\cos\theta} + \Delta L}{v}, \tag{2.5}$$

where v is the speed of light inside the medium, θ is the beam propagating angle, L is the thickness of the medium and ΔL is the increased photon path due to scattering.

2.2.1 Monte Carlo simulation

To evaluate the light path inside the medium, there are a few tools such as the diffuse theory and Monte Carlo are developed to simulate the light-tissue interaction. The diffuse theory is a simplified version of radiative transport equation (RTE), it is an analytical model for the light migration problem. However, the diffuse theory is valid only when the medium scattering coefficient is way more significant than the absorption coefficient (μ_s'»μ_a). Monte Carlo is used to resemble the photon propagation inside the medium when both the scattering and absorption properties are considered. Monte Carlo neglects all wave natures and treats photons as particles. Monte Carlo is a numerical approach based on random walk, it does not require simplification, and it provides a result for one specific case at a time. It does require an extensive computing capacity as the computer has to process a large number of photon packages to obtain the necessary statistics. One simulation can comprise several millions to billions of photons.

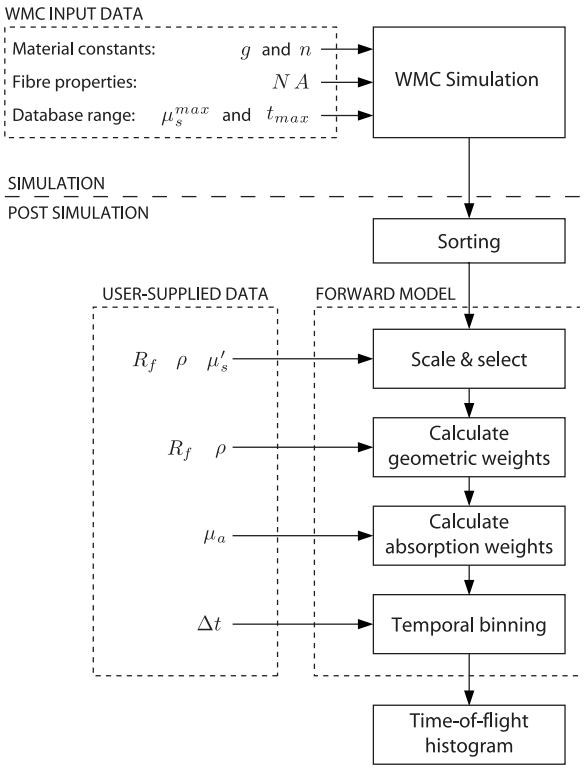

FIGURE 2.5: A flowchart of white Monte Carlo model, cited from Alerstam et al. [10]. A few input parameters can be used to generate and rescale the database.

White Monte Carlo

As mentioned above, heavily computational progress is essential for running Monte Carlo. White Monte Carlo (WMC) was then developed to save the computing time

[11] [12], one simulation of WMC is a combination of a wide range of optical properties with proper rescaling [10]. The light paths are only determined by the phase scattering function and a sequence of random numbers [10] in a non-absorptive homogeneously turbid medium. The scheme in figure 2.5 illustrates the WMC model. Users can input few parameters to generate a database, that include the material anisotropy factor g, the refractive index n, the fiber numerical aperture NA, the maximum scattering level μ_s^{max} for the simulation and the stop time t_{max}. Then the database is sorted and stored and sent to the forward model. Based on the user input parameters for the forward model, the database is then rescaled, and a corresponding time of flight histogram is generated. Those parameters are the radius R_f of the incoming beam, separation distance between detector and source ρ, reduced scattering coefficient μ_s', absorption coefficient μ_a and desired temporal channel width Δt [10][13]. During this thesis work, the databases were compiled by previous Biophotonics group members for intralipid in an infinite geometry[10]. The photons were simulated at $\mu_s = \mu_s^{max} = 90$ cm^{-1}, μ_a = 0 cm^{-1}, $t_{max} = 2$ ns, NA = 0.29, n = 1.33, g = 0.70 and 2×10^8 photons. Photons are terminated in the simulation if the time of flight exceeds the t_{max} or they left the medium.

2.2.2 Photon time of flight spectroscopy

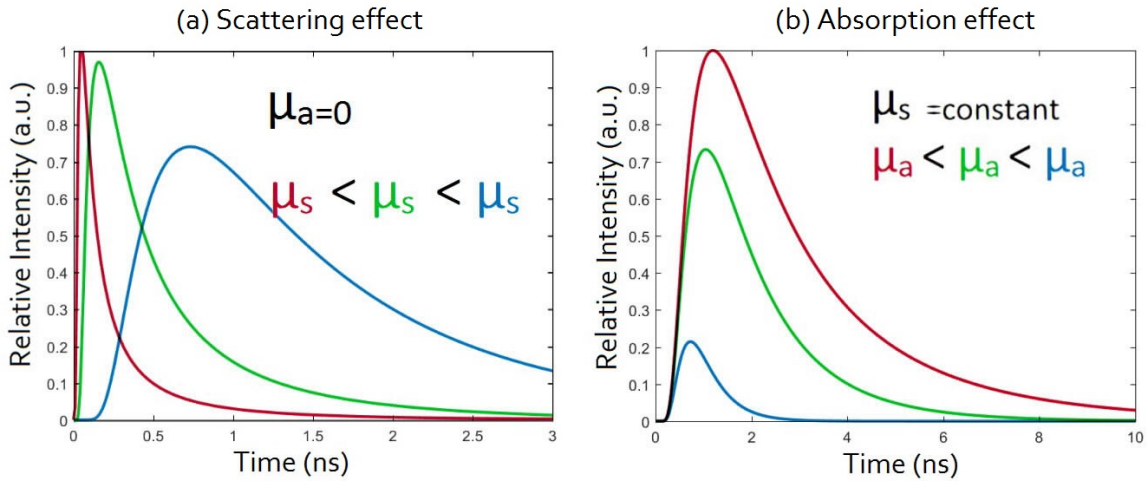

FIGURE 2.6: A laser pulse is broadened inside a turbid medium. The sub-figure (a) shows how the scattering coefficient affects the pulse shape and sub-figure (b) shows the absorption effect. PTOF is for analyzing scattering media, thus for any test object it must contain a certain amount of scattering property.

When light propagated through a turbid medium, diffused photons lost their initial information and traveled a longer path than ballistic photons. The principle of PTOF is to inject a sharp laser pulse into the turbid medium, the shape of the resulting time of flight distribution depends on the medium optical properties, as shown in figure 2.6. Due to multiple scattering events inside the medium, the resulting pulse is

much broader than the initial pulse. Increase the scattering coefficient would cause the photons undergo more scattering events, the average photons take a longer path, cause the peak of PTOF signal profile shifts to the later time (to the right in figure 2.6). More scattering events meaning more photons could be absorbed during the propagation, thus the peak intensity would decrease. Increase the absorption coefficient will increase the absorption rate and lower the light intensity, the PTOF profile shifts to the earlier time (to the left in figure 2.6) as more late photons are absorbed.

However, to record the profile of delayed pulse in one cycle is very challenging. The laser pulse width used for PTOF is usually in picoseconds scale. To be able to resolve the photon distribution, the detector must be extremely fast to such an extent. Such a detector is very costly and does not have an excellent temporal resolution. Instead of performing a direct pulse profile recording, a technique name time-correlated single photon counting (TCSPC) was used, it is also known as photon time of flight spectroscopy. In this technique multiple short laser pulses are sent into to a turbid sample, a single or no photon is registered for each pulse at the detector to build up a photon arrival time histogram. The profile of the histogram represents the laser pulse broadening. By fitting the broadened pulse with the database, the turbid medium absorption and scattering information can be extracted.

2.3 Ultrasound optical tomography

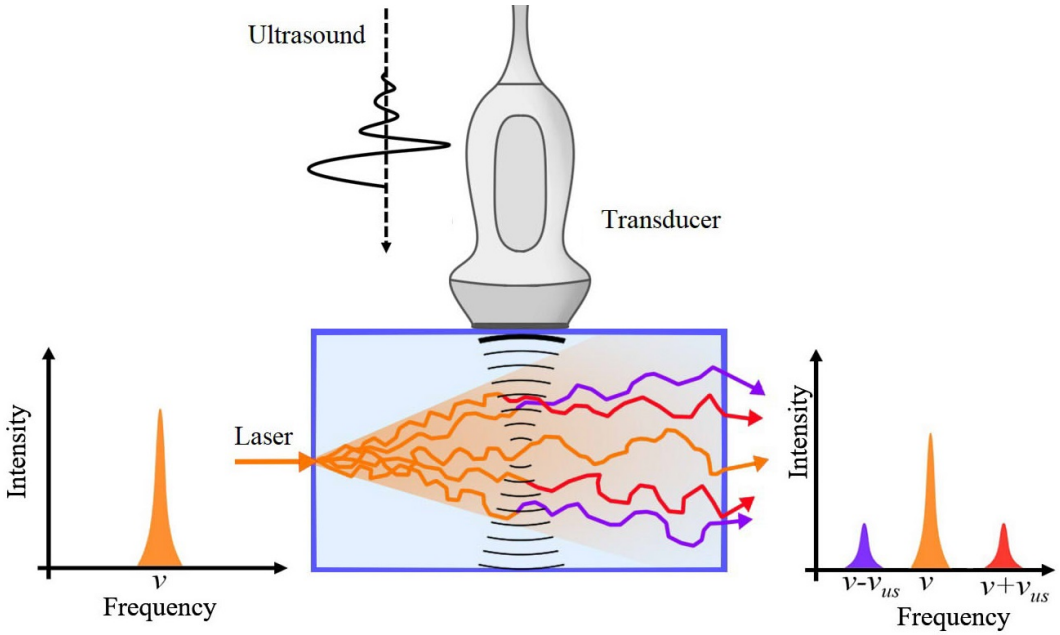

FIGURE 2.7: Schematic of the ultrasound optical tomography principle.

Ultrasound optical tomography is based on the acousto-optic effect. When an ultrasound is applied to a biological tissue, see figure 2.7, the ultrasound wave will modulate the refractive index of the medium and turn it into a phase and amplitude grating. For any incoming light diffracted on the grating, the diffracted light frequency is shifted by one or multiples of ultrasound frequency. The first order sideband (two frequency bands on either side of the carrier wave) shifted by one ultrasound frequency contains the most number of modulated photons, those photons are named the tagged photons. Tagged photons intensity is dependent on the target optical properties, and the focused ultrasound volume indicates the origin of these tagged photons[14]. It is possible to map the light spatial distribution within the medium by scanning the ultrasound focus, the resolution of the map is dependent on the ultrasound focus size.

2.3.1 Ultrasound and focus

A commercial ultrasound machine EPIQ7 from Philips was borrowed from Biomedical Engineering, LTH. Ultrasound is a sound wave in a high-frequency region that excesses the upper audible limit of human hearing.

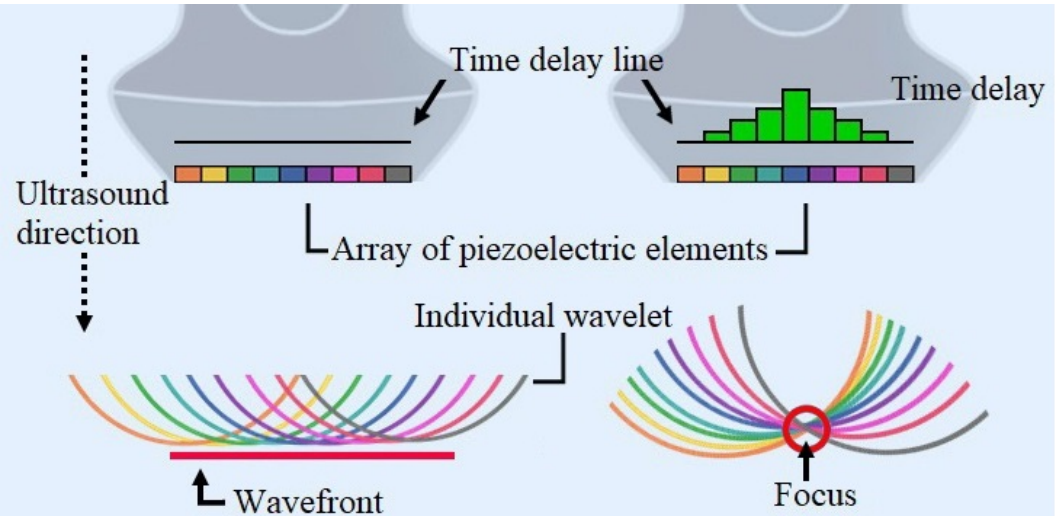

FIGURE 2.8: Schematic diagrams show how to form a transmission focus for a phased array transducer. The principle of forming a high amplitude pulse at the focus is by delaying pulses from elements that are in the middle of the array, so all pulses from all elements arrive at the same location at the same time.

The principle of how a phased transducer forms an ultrasound focus is shown in figure 2.8. The front of the transducer is made up of many piezoelectric elements that emit spherical waves. The sum of all spherical waves at each distance determines the present pressure amplitude. Since each spherical wave has a different phase, they interfere constructively and destructively to achieve a maximum and

minimum amplitude at different locations. Piezoelectric elements can convert electrical pulses into ultrasound pulses. Conversely, it converts ultrasound feedback echo into electrical signals. To increase the pressure amplitude and acquire more extensive echo feedback at the desired focus, pulses from all elements must arrive at the location at the same time to concentrate the pressure power. Both are achieved by electronic delays, see figure 2.9 and figure 2.10. The principle of forming US wave front and focus are the same for linear and phased array transducers, except the scan line for phased array transducer can be oblique.

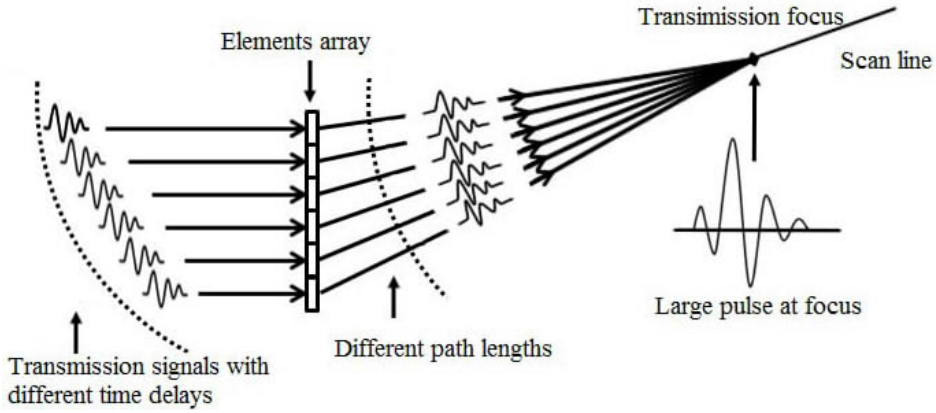

FIGURE 2.9: Creating a transmission focus for a phased array transducer. When pulses from all elements arrive at the location at the same time, a large pulse would be formed. The further the element is from the focus, the earlier it emits a pulse.

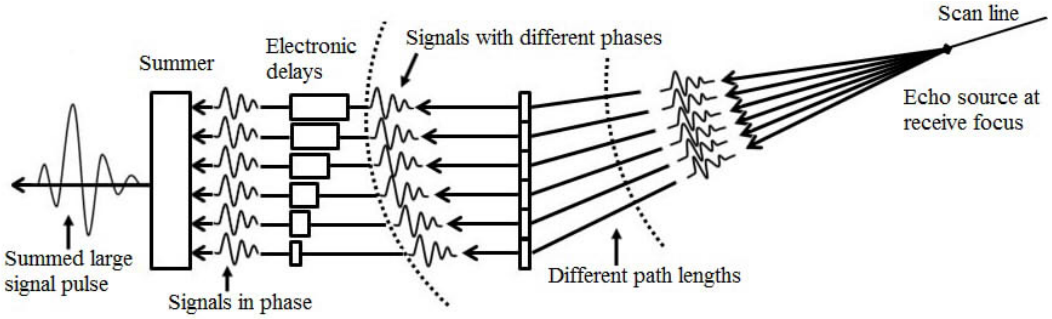

FIGURE 2.10: Creating a receive focus for a phased array transducer. The closer the element is to the receive focus, the earlier the pulse reaches the element, which means a longer electronic delay is required to obtaining a large echo signal at the summer. The delays are chosen in such a way that the travel time of a sound wave plus the electronic delay is the same for all elements. A large echo signal is obtained by summing all in phase echo signals.

The longitudinal resolution of an ultrasound focus is dependent on the ultrasound pulse length. Have a short pulse would result in a high longitudinal resolution. However, less number of photons would be tagged, and higher sensitive detection is required.

2.3.2 Acousto-optics

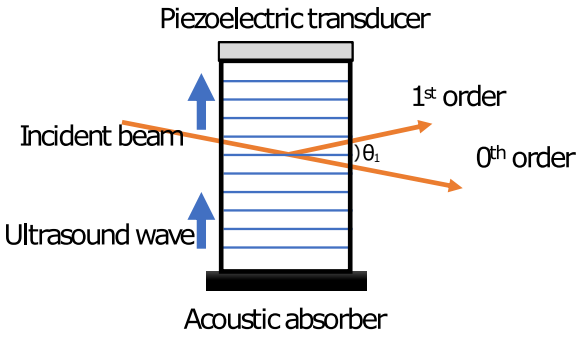

FIGURE 2.11: An illustration of an acousto-optic modulator. Piezoelectric transducer generates acoustic wave that modulate the refractive index of the crystal.

An acousto-optic effect is known as the diffraction of light by ultrasound waves. When an ultrasound wave enters a medium, it changes the medium's refractive index by pressure fluctuations. When the light wave interacts with this refractive index grating, light can be diffracted into several orders (Only 0th and 1st orders are showing in the figure 2.11). If the incoming ultrasound frequency is denoted as f_{US}, the wavelength of the ultrasound is:

$$\Lambda = \frac{v}{f_{US}}, \tag{2.6}$$

where v denotes the propagation speed of ultrasound inside the medium, and Λ is the acoustic wave wavelength. The generated refractive index grating has a period of Λ, and the light diffraction pattern dependent on the diffraction angle θ_n, see figure 2.11, which is dependent on both light wave and sound wave wavelengths:

$$\Lambda \sin(\theta_n) = n\lambda, \qquad n = 0, \pm 1, \pm 2, ... \tag{2.7}$$

where λ is the light wavelength, n is an integer diffraction order. The frequency of the diffracted light is shifted by multiples ultrasound frequency due to Doppler shift:

$$\Delta f = n \times v_{US}. \tag{2.8}$$

The most common application of the acousto-optic effect is the acousto-optic modulator (AOM), it is used for frequency modulation, pulse control, time switching and more. Two AOMs were used in the UOT setup, one AOM was used to pulse the pump beam to burn the spectral hole, and the other AOM was used to pulse the probe beam to interact with the tissue phantom.

2.3.3 Acousto-optic imaging

UOT project is based on the acousto-optic effect. The first order sideband in figure 2.7 is the target of interest. The basic idea of acousto-optic imaging is by recording the number of tagged photons while moving the ultrasound focus around. Figure 2.12 shows one simple case of how to map a 2D image with the help of ultrasound. When the ultrasound focus locates a region with no diffused light, the number of tagged photons should be zero. Once the ultrasound focus enters the diffused light region, the number of tagged photons is corresponding to the light irradiance inside the ultrasound focus. When ultrasound focus comes across an absorber, the light irradiance will decrease, resulting in a reduction of tagged photons quantity.

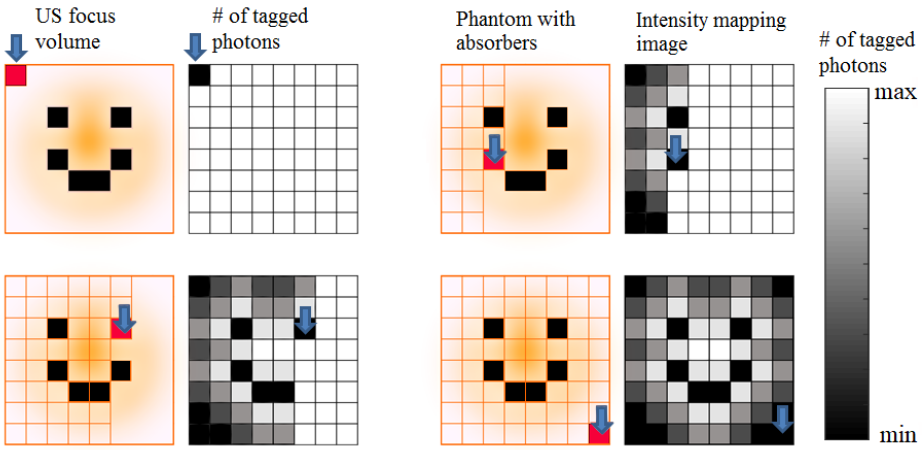

FIGURE 2.12: A scattering sample with absorbers implanted inside is undergoing an acousto-optic imaging. The number of tagged photons is proportional to the light irradiance inside the focus. The yellow glowing color represents the irradiance of the light inside the medium.

2.3.4 Basic principle of spectral hole burning

During the UOT measurement, it is essential to filter out the untagged photons to decrease the background signal. However, conventional bandpass filter does not have enough finesse to filter out the tagged photons. The spectral hole burning technique is used to create an ultra-narrowband filter, it can block the untagged photons to enable a direct measurement of the shifted frequency.

The spectral hole burning filer used in this thesis was prepared by my colleague Di M.Q.[15]. The spectral hole is created in praseodymium (Pr^{3+}) doped Yttrium silicate crystal (Y_2SiO_5). The doped crystal is stored in a vacuum chamber with a temperature around 2.17K. The idea of spectral hole burning is by exciting the ions to more highly excited states and then having them delay to other hyperfine levels of the ground state, it will prevent the ions to respond to the original frequency, and

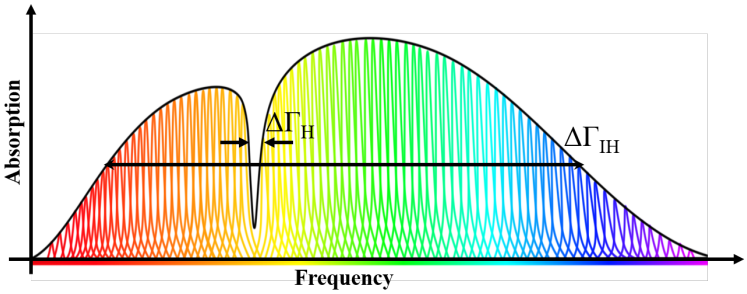

FIGURE 2.13: The inhomogeneous absorption profile is indicated by the black line in the figure, and it has a bandwidth $\Delta\Gamma_{IH}$. The inhomogeneous profile is made up of a series of continuum boarded homogeneous lines. The transition frequency of each ion is slightly shifted due to the crystal environment, results in the broadened profile. A laser can be used to create a spectral hole in the interval $\Delta\Gamma_H$, light with the frequency of the hole will undergo the minimum amount of absorption (the figure is not to scale).

the total absorption at this frequency will decrease, figure 2.13 shows an example of spectral hole filter. The way of applying the spectral filter to the UOT signal is explained in figure 2.14.

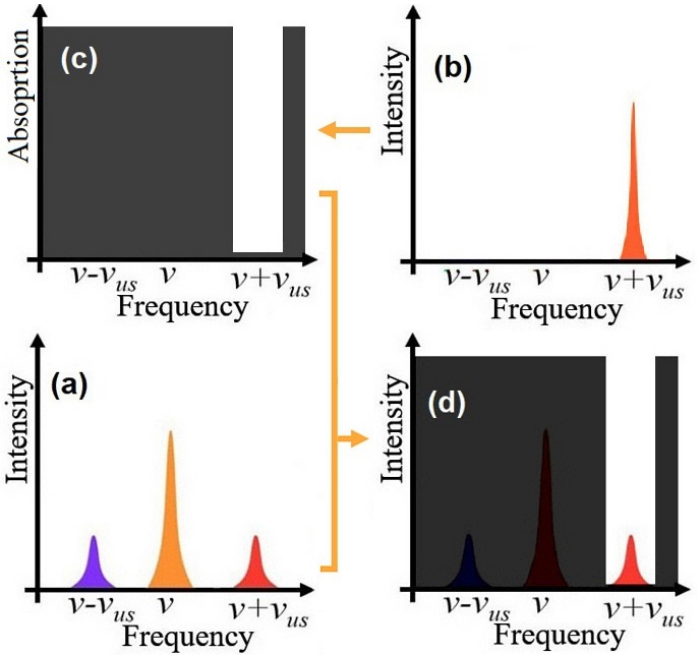

FIGURE 2.14: (a) US modulated signal (continuation from figure 2.7), including the signal carrier (at v) and two first order sidebands (at $v \pm v_{us}$).(b) The pump laser center frequency is shifted to $v + v_{us}$ and it is used to burn the spectral hole filter. (c) Apply the spectral filter to the modulated signal. (d) Tagged photons from the first positive sideband is filtered out.

Chapter 3

Experiment

3.1 Tissue-mimicking phantom preparation

Due to the complexity and risks of testing developing medical diagnostics on patients, tissue models are developed to evaluate the theoretical predictions. It mimics the structural and optical properties of the actual biological objects. The most straightforward approach of characterizing a tissue phantom with known optical properties is by mixing known proportions of pure scatterer and absorber.

3.1.1 Optical characterization of a homogeneous liquid phantom

The tissue model optical parameters should be able to be predicted by knowing the compositions and constituents' characteristics. The liquid phantom is the simplest tissue model to start with, and it has very high flexibility regarding changing the absorption and scattering properties. Distilled water is used as the base for a liquid phantom, then the absorbers and scatterers are suspended in the water. Water is transparent and non-scattering, it has a relatively low absorption coefficient in the visible wavelength region (at 606 nm, $\mu_a = 0.0026$ cm^{-1}[16]).

As mentioned in the theory section, intralipid 20% from Fresenius Kabi AB, Uppsala was used as the pure scatterer. As a pharmaceutical product used for parenteral nutrition. Intralipid consists of small fat droplets suspended in water that make it a highly scattering solution. Driver et al. [17] suggest 75% of the droplets in the intralipid have diameters smaller or equal to 125 nm.

Indian ink is commonly used as an absorber for a liquid system, it is neither toxic nor fluorescent, and it has a long

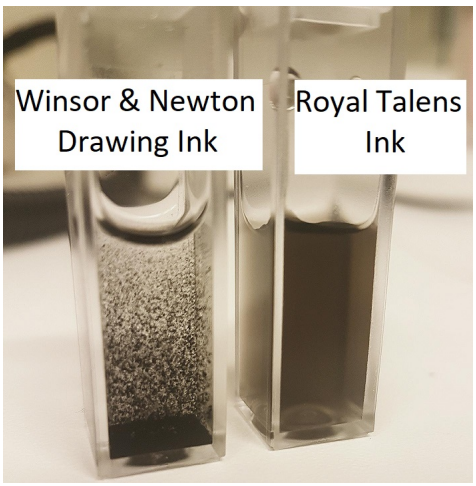

FIGURE 3.1: 30 minutes in, a strong sedimentation problem was observed for water-based ink sample.

preserving time. However, unlike intralipid, Indian ink does not have a controlled production condition, and there is no standard absorption coefficient of ink for any brand or batch. Large ink particle scatters visible and near-infrared red light. Water-based ink has a very strong sedimentation problem. 'Waterproof' Ink from Royal Talens was used, it does not have the diffusion problem, but it was quite difficult to dissolve them in water. A pre-diluted batch solution (1:100) of the Royal Talens ink was prepared to solve the problem. Meanwhile, 2 hours ultrasound bath was also applied to the pre-diluted (1:100) ink solution to break the large suspended ink particles. In figure 3.1, two different types of ink solutions were prepared by the same procedure and proportion. The sedimentation problem started appearing for water-based ink (Winsor & Newton) after 10 minutes, while it took two weeks or even longer for the waterproof ink to begin sedimenting.

Two different methods were used to determine the absorption coefficient of the pre-diluted ink solution (1:100). Collimated transmission spectroscopy (also known as the absorption spectroscopy, ABS) was the first approach. Colleague Di M.Q.[15] performed the ABS experiment to determine the prepared ink solution (1:100) absorption coefficient. Her experiment result suggests,

$$y = 0.933 \times x, \tag{3.1}$$

where y is the ink absorption coefficient [cm^{-1}] and x is the ink concentration in total volume [%]. The photon time of flight spectroscopy was used as the second approach of determining the ink absorption coefficient, the detail of this method is presenting in section 3.1.3. The measured ink absorption coefficient by these two different methods were compared in the result section 4.1.1.

3.1.2 Convert liquid phantom to solid phantom

A liquid phantom with known optical properties is prepared by mixing proper amounts of intralipid and ink solution (1:100). The advantage of a liquid phantom is that its properties can be varied easily, and that probe/detector can move freely within the medium. However, a fluid form model cannot mimic the macroscopic geometry of a tissue sample, and it cannot hold a physical shape as an individual.

Making a solid tissue mimic phantom would be a better approach. It can be more geometrically complicated with impurities implanted. Particles inside the solid phantom would experience the minimum amount of sedimentation problem. A good solid phantom for the UOT should have controlled and stable optical and mechanical properties, a near perfect matching interface between impurity and the surrounding. Also, more important, it should be aqueous to enable ultrasound propagation inside with minimum amount of US power loss.

Agar powder (A7921, SIGMA) was used to convert the liquid phantom into solid form, and it forms a transparent aqueous gel with water. It can hold water together is due to the presence of hydrophilic groups in the polymer chain (OH, -COOH, -$CONH_2$, y-SO_3H [18]). Just like the liquid phantom, agar phantom optical properties can also be predicted from the individual characteristics of scatterer and absorber. Rinaldo C. et al. [19] suggest 1% of agar powder is enough for hardening the phantom, as higher concentration gives a high viscosity of the solution which makes it difficult to dissolve and mix the components.

3.1.2.1 Procedures

4 g of agar powder was mixed with 400 mL of distilled water in a glass beaker. To avoid inhomogeneous heating, a magnetic stirring bar was put inside the glass beaker, and together they were water bathed in a larger beaker on a hot plate stirrer (AREX Digital CerAlTop). External digital thermoregulator was connected to the stirrer to provide direct temperature control. The mixture of agar and water was heated to 95 C°, and the solution was stirred with the magnetic stirring bar at a constant speed for 2 hours. The opening of the breaker was sealed off with an aluminum foil to minimize evaporation, and the stirring speed was set to a reasonable high value without form bubbles or whirls. As the agar powder dissolved completely, the mixture solution turned transparent. Then the heating was set to 45 C°, the stirring continued. An appropriate amount of ink and intralipid were added into the agar solution when the temperature was around 45 C°. After stirring for 30 minutes, the heating was turned off, and the mixed agar solution was transferred into a cylindrical mold and solidified at room temperature.

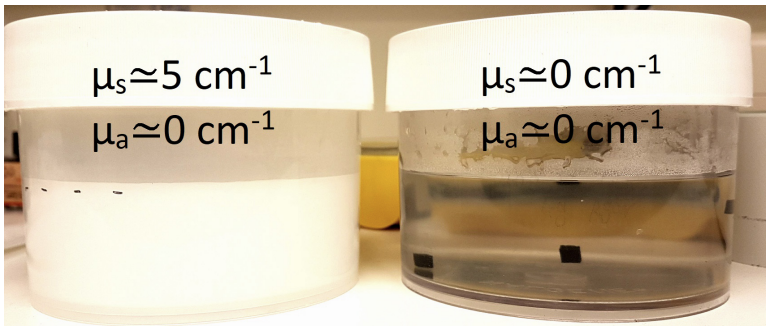

FIGURE 3.2: The agar phantom on the left has a higher scattering property and the other agar phantom has almost no scattering. Both phantoms have impurities implanted inside. The impurity is also agar gel but with absorption coefficient around 90 cm^{-1}, the impurity dimensions are 5 mm x 5 mm x 5 mm (The upper white parts are the lids on the two molds).

To be a more accurate representation of biological tissue, impurities are implanted into the phantom to simulate an ailing biological sample. The impurity can also be agar gel but with different optical properties. If an impurity needs to be inserted into the agar phantom, there are two approaches. One way is solidifying the phantom

layer by layer: pour a certain amount of mixture agar solution into the mold and let it naturally hardens, while keeping stirring the rest solution in the water bath at 45 C°. Place the impurity on the solidified agar gel then carefully pour the rest of solution into the mold and let it cools at room temperature. This method is very time consuming, but in exchange, the impurity is correctly placed at the desired location. The second method is placing the impurity during the aqueous gel solidifying progress. A thin needle can be used to push the impurity from the surface of the solidifying gel into desired depth, the temperature of the mixture is generally around 38 C°. This method is quick, but it requires to be good at judging the timing. If the gel is not viscous enough the impurity will not stay at the required location, if the gel surface is already solidified, forcing in the impurity would damage the interface and structure. Using either of the methods must be careful in avoiding forming bubbles. The second method would not work well if the agar gel is highly scattering or absorbing, as the impurity location optical information is lost during multiple scattering and absorption events, an example is presenting in figure 3.2.

All solidified phantoms should be sealed and stored in a water tank in a refrigerator (temperature around 10 C°). The agar phantom can be used for measurement after being cooled at least 12 hours. PTOF was also used to analyze the manufactured agar phantom optical properties.

3.1.3 Photon time of flight spectroscopy

When a short laser pulse (on the picosecond scale) is sent into a scattering medium, the light experiences multiple scattering events, that cause the pulse profile broadened in time. By fitting the pulse curve with the WMC database, the optical properties of the medium can be deduced. The optical properties of intralipid 20% and ink base (1:100) were both examined by the PTOF spectroscopy. Since intralipid has a standard reference value in scattering coefficient, the reduced scattering measurement result can also be used to test the precision and accuracy of PTOF.

3.1.3.1 Experimental Setup

A pulsed supercontinuum fiber laser (Model SC500-6, Fianium, UK) was used as the light source, it has a repetition rate of 80 MHz, and it can generate 6.0 ps long pulses (500-1850 nm). The output light was coupled into an acousto-optic tunable filter (AOTF, SN101571). There are two crystals inside the AOTF housing; VIS crystal covers the wavelength range 400-700 nm and NIR1 crystal covers the wavelength range 650-1100 nm. The acousto-optic tunable filter (AOTF) was used to select a spectrally narrow pulse, and the selected pulse bandwidth is about 3 nm when the wavelength is below 650 nm, and it increases to 6 nm at 1100 nm. A narrow-core fiber (10 μm, SMF-28) was coupled to the output of AOTF, and the light was sent to a beam splitter.

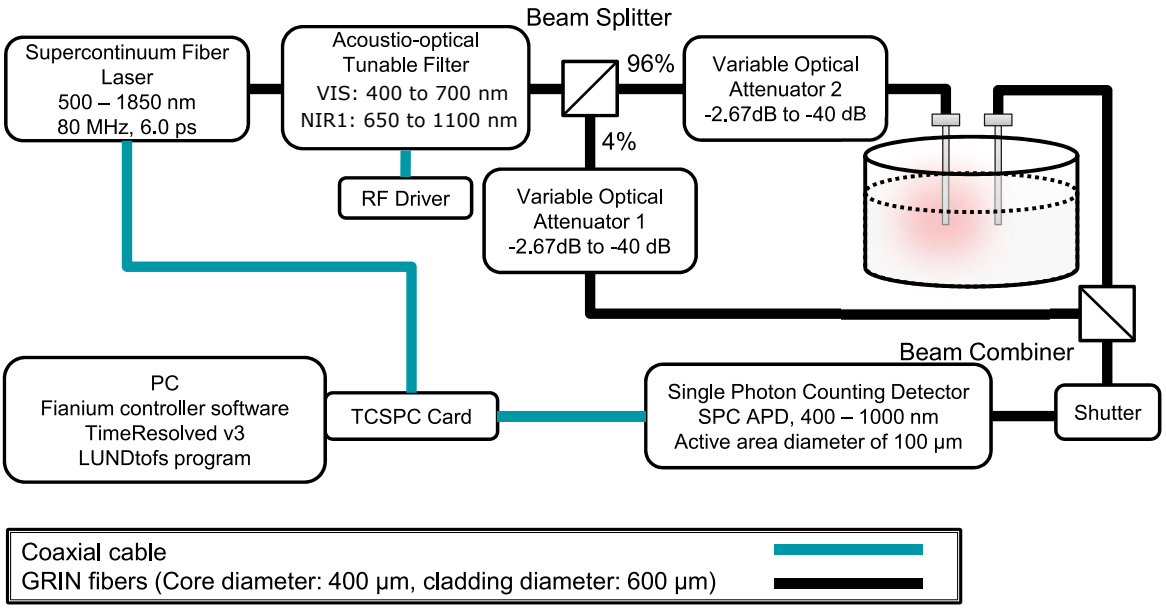

FIGURE 3.3: Schematic arrangement of the PTOF setup. PTOF is capable of measuring sample absorption and reduced scattering coefficients the same time. If a light pulse is sent through a turbid medium, and the pulse will be broadened based on the statistical distribution of each detected photon's optical path.

4% of the initial light pulse was severed as the time reference, and 96% of light was sent to the testing sample. Each beam path contains a variable optical attenuator (FVA-3100, OZ Optics Ltd), they were both remotely controlled by computer within attenuation range -40 dB and -2.6 dB. Attenuators were used to adjust both beam paths pulse power to achieve single photon detection for the time of flight system. The 96% of light through the attenuator was coupled into a custom needle fiber. The needle fiber was inserted into the phantom, and the diffused light was collected by the second needle fiber and combined with the reference light. Both needle fibers were placed in parallel and kept at the same level. If a container was used to store the tissue phantom, its wall must be covered by black tape or paper to minimize the reflection from the wall surface. The separation distance between the two fibers are adjustable, but usually, it was kept at 20 mm as the WMC database was calibrated for a separation distance of 20 mm. The collected sample PTOF signal and the time reference pulse were combined at the beam combiner. A single photon counting avalanche photodiode detector (PD1CTC, Micro Photon Devices) was used for the visible wavelength range detection. The APD was connected to a TCSPC card (SPC-130 Becker & Hickl, Berlin, Germany) to acquire the PTOF signal distribution.

3.1.3.2 Procedures

Depending on which wavelength is going to be used, the SMF fiber of VIS or NIR1 should be coupled to the beam splitter. In this thesis work, the manufactured tissue

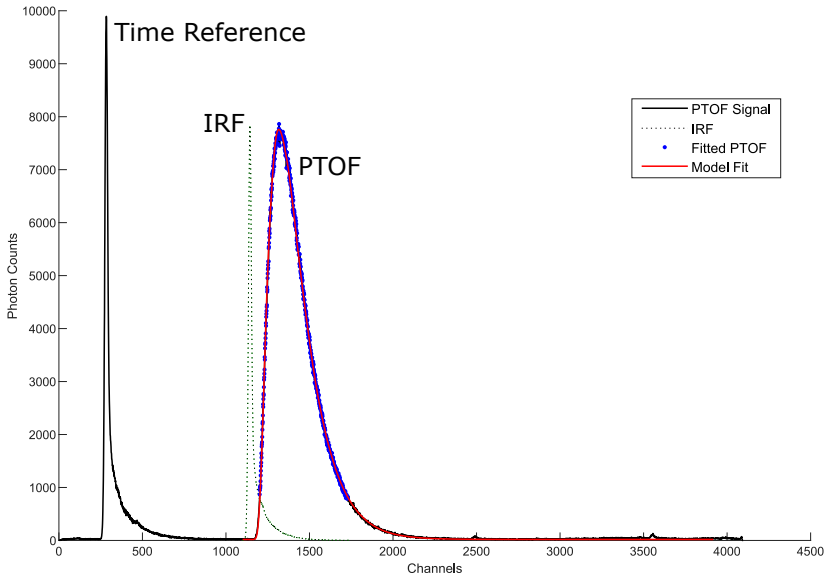

FIGURE 3.4: An example of measured PTOF signal and time reference with a model fit. Each channel corresponds to 3.0538 ps.

phantom optical properties at 606 nm were of interest. The SMF fiber of the VIS output was coupled to the beam splitter, and the NIR1 output was blocked. RF input for the AOTF was also changed to VIS. The laser, detector, shutter, and attenuators were turned on. The light source amplifier enables key was turned on (switch from 0 to 1) after the laser had warmed up, the laser power was increased to 100 % and set to PC control mode. On the computer, Fianium AOTF controller software was used, the visible spectrum range was selected, and its calibration file was loaded manually. PTOF does not require very strong laser light ($\approx$ 20 mW from the SMF fiber at 606 nm was enough), but if the light comes out of the probe fiber is too weak, it could be due to misalignment from the AOTF output. Each AOTF output has a manipulator, in which the fiber is inserted to couple with the AOTF output. One can position the output fiber to a power meter and adjust the four adjustor screws to align the coupling fiber.

LundTOFS software was first used to have a safe startup of the time of flight system, both time reference, and sample attenuation was set to -40 dB. Then LundTOFS was used to turn on the AOTF, and wavelength 606 nm was chosen. By changing the attenuation values for both time reference and sample, two signal peaks can be observed in the oscilloscope mode of the software, the height on the left side represents the time reference, and the peak on the right side represents the sample signal, see figure 3.4. The TCSPC card contained a constant fraction discriminator (CFD). When photons reached the detector, the signal will be sent to the CFD first. It is used to minimize the signal amplitude fluctuations. The attenuations of both time reference and sample were adjusted, both signals should have almost the same height

and their total photons counts per second should not exceed $1.0{\cdot}10^5$ photons/s. After finished the sample measurement, a double-sided thin black paper was inserted between two fibers, and this was used to perform the instrument response function (IRF) measurement. The incoming laser pulse is not infinitely narrow, and after it traveled through multiple optical components the laser pulse was broadened (usually ≈ 80 ps). A thin piece of black paper has a relatively small amount of scattering, and it is used to mimic a tissue sample that has an extremely small temporal broadening.

Timeresolved v3 Matlab software was used to evaluate the absorption and reduced scattering coefficients of the acquired data. After both the IRF and sample files were imported to the Timeresolved v3, the White Monte Carlo model was chosen. Different data templates are available within the program, in this thesis work, template intralipid-finite.mat was used; the photons were simulated at $\mu_s = \mu_s^{max} = 90$ cm^{-1},μ_a = 0 cm^{-1}, $t_{max} = 2$ ns, NA = 0.29, n = 1.33, g = 0.70 and $2{\times}10^8$ photons. The 4% of the light fraction was used to sync the IRF and PTOF measurements that were taken at different times. The theoretical model was first convolved with the IRF pulse, and then the convolved pulse was used to try to fit with the broadened PTOF pulse by iteration process of some combinations of μ_s' and μ_a.

3.2 Ultrasound focus experimental setup

An EPIQ 7 ultrasound machine from Philips was borrowed from Biomedical Engineering, LTH. As a commercial product, it was easy to operate, and its maximum US output is always below the safety limits. However, it came with the disadvantage of limited access one has towards the operating software. The US scanner cannot be triggered by an external trigger. Instead, it has a US output trigger, which was later used in UOT setup to trigger the laser sequence, see figure 3.5. A US scanner is mostly known for performing a B-mode (Brightness) imaging, and it displays a two-dimensional image of US echoes in brightness. The returned echo signal amplitude determines the echo brightness. However, B-mode imaging was not the setting that was of interest in the

FIGURE 3.5: The US scanner borrowed from LTH, EPIQ 7, Philips. The coaxial cable highlighted by the red circle is the output trigger.

UOT project. Two US modes can form a US focus, M-mode (Motion display, commonly used to view a mono-dimensional presentation of a heart) and PW-mode (Pulsed wave Doppler, commonly used to trace blood flow). Both modes have high repetition rate. M-mode displays the chosen US line in time motion, PW-mode positions the US focus at any point along the US line and detect the returned signal. Due to background scanning (B-mode) cannot be stopped while running the M-mode scan, PW-mode was used to assist the UOT project, and its US focus properties were investigated.

3.2.1 Experimental Setup

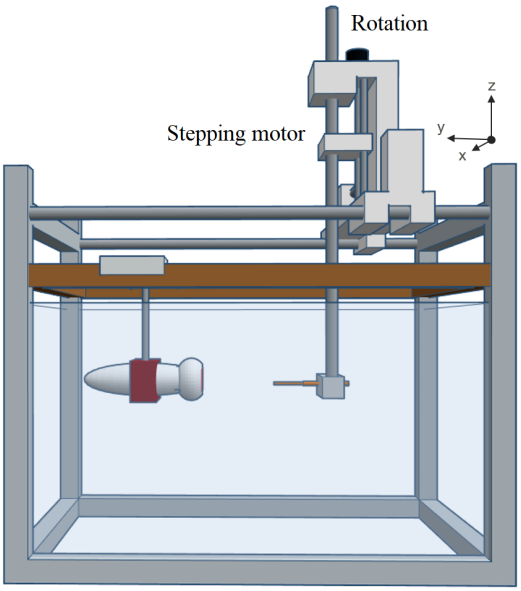

FIGURE 3.6: Partial computer-controlled hydrophone measurement system. A stepping motor was used for positioning the hydrophone inside the water tank, its measured signal is then read out by an oscilloscope and sent to a computer.

A water tank was filled with deionized water, and the walls were partly covered with acoustic absorber material to minimize the US reflections. The X5-1 transducer was mounted horizontally on a holder and placed into the water tank. A needle hydrophone (HP series, SN 1025) was used for the US pulse measurement, and it can measure the US in the frequency range 10 kHz to 60 MHz, its sensor diameter is 0.5 mm. The hydrophone readout output was plugged into a submersible preamplifier with a 50 Ω output impedance, and then an enhanced signal was read out by an oscilloscope and analyzed by a computer. A stepper motor was used to position the hydrophone in three orthogonal directions inside the water tank, and the stepper motor can perform an angle rotation with 0.2 $^\circ$ resolution and move in three axes with a minimum step size of 10 μm. Software implemented in the LabVIEW was used to control the step motor and analyze the readout US signal. The transducer

and hydrophone were first aligned, then the hydrophone was moved numerically to measure the US amplitude distribution in a cross-section.

3.2.2 Procedures

The most complicated and time-consuming part of the measurement procedure was the positioning and alignment of the transducer and hydrophone. As described in the experimental setup, the transducer was mounted in a fixed position while the hydrophone was mounted on the stepper motor. The principle of the alignment was

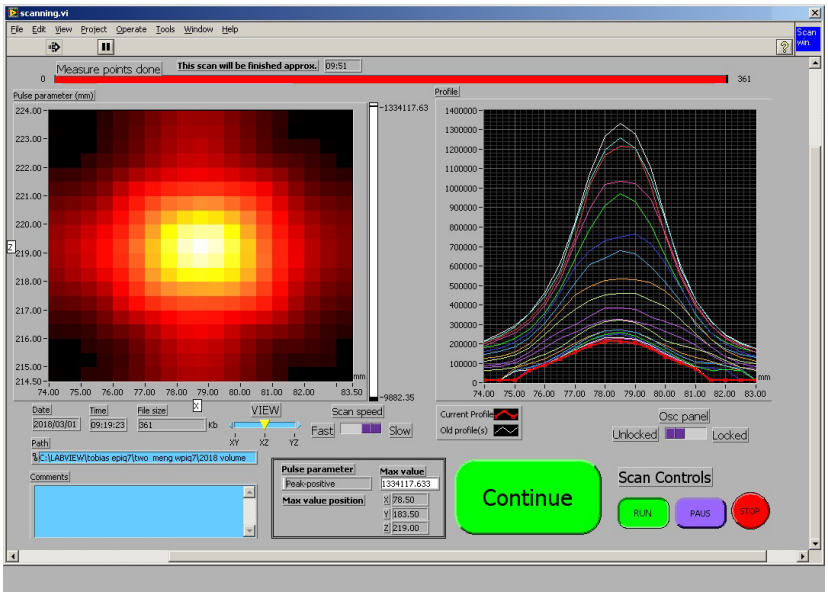

FIGURE 3.7: An example of the US focus profile plot from the LabVIEW measure window.

based on the changing positioning of the hydrophone between near field (typical ∼2 cm) and far field (typical ∼15 cm) to the transducer in the y-direction (see figure 3.6). The US focus should always be positioned on the tip of the needle hydrophone during alignment, the way of doing it is by switching the US to B-mode scan, under this setting the outer shape of the hydrophone was visible on the display screen of the scanner. The US focus was then repositioned onto the tip of the hydrophone along the y-direction, US scanner was then set to PW-mode. The hydrophone was first moved to the near field to the transducer and scanned in both x and z directions to find the highest amplitude spot, and this spot was the new center position of the hydrophone. Then the hydrophone was moved to the far field, then it was tilted and rotated with a small step size of an angle to find the maximum signal readout, a new x-z directions scanning was performed, and the hydrophone was repositioned to the highest signal spot. This alignment was performed two or three times to confirm the US propagation direction was aligned with the positioning system (figure 3.7 shows a good alignment). The measurement started when all the air bubbles inside the

water tank is disappeared. For each pixel in figure 3.7 the full temporal profile of the US pulse is stored.

3.3 Ultrasound optical tomography

High scattering and high absorption properties of tissue limit most of the optic-based diagnostic methods. In contrast of UOT, US can penetrate deep into the tissue, but the laser intensity reaches the region of interest is relatively low, and the tagged light from the small focused US volume are many orders of magnitude weaker than the carrier. A high finesse filter is a key to achieve the success of UOT development. Such a filter should have the highest possible etendue, sharp frequency edge, be stable and long-lived (or permanent).

The optical transition $^3H_4 \Rightarrow ^1 D_2$ of Praseodymium (Pr^{3+}) ions in Pr^{3+}:Y_2SiO_5 at 2.17 K, 605.98 nm, was used to prepare the spectral filter by colleague Di M.Q.[15]. 606 nm is not an ideal wavelength for deep tissue penetration, e.g., both Hb and HbO_2 show strong absorption at this wavelength. Using a wavelength from the optical window region with low tissue absorption can increase the light penetration depth, but the problem due to tissue scattering can only be solved by using a high finesse filter with high etendue. The prepared spectral filter has ideal etendue of 4π steradian (solid angle of all space), but if consider the crystal geometric shape and incoming light angle, the solid angle of one face of a cube is $4\pi/6 = \frac{2\pi}{3}$ steradians (a cube has six identical faces). The prepared spectral filter has a lifetime of 1 s (without magnetic field), 1 MHz bandwidth with a 50.4 dB suppression ratio (on/off absorption ratio over different frequencies inside the spectral region). Polarization D_2 was used for both probing and spectral pumping due to the cryostat geometry limitation, see Appendix A.1.

3.3.1 Experimental Setup

The experimental setup is presented in figure 3.8, a highly stabilized Rhodamine 6G dye laser [20] sent around 40 mW light through a single mode fiber onto another optical table. The output laser from the fiber has a diameter of about 2 mm, and a beam expander was used to reduce the beam diameter to 1 mm. A beam splitter split the beam into two with a splitting ratio of 10:90. The 10% of light was sent into a photodiode (Thorlabs, PDA10BS), it is the reference detector for both intensity and time. The 90% light was sent into the first AOM (Isomet, 1205c-1), the AOM acted like a switch between two operating modes: (1) spectral hole pumping/erasing and (2) UOT probing. The 1st order of beam out of the first AOM was used as the pump, and the 0th order beam is used as the probe. The AOMs were controlled by the RF signal from a signal generator, while the signal generator was controlled by the arbitrary waveform generator. When the first AOM was on, 80% light went to the 1st order, and the beam was then expanded and collimated to 10 mm diameter to

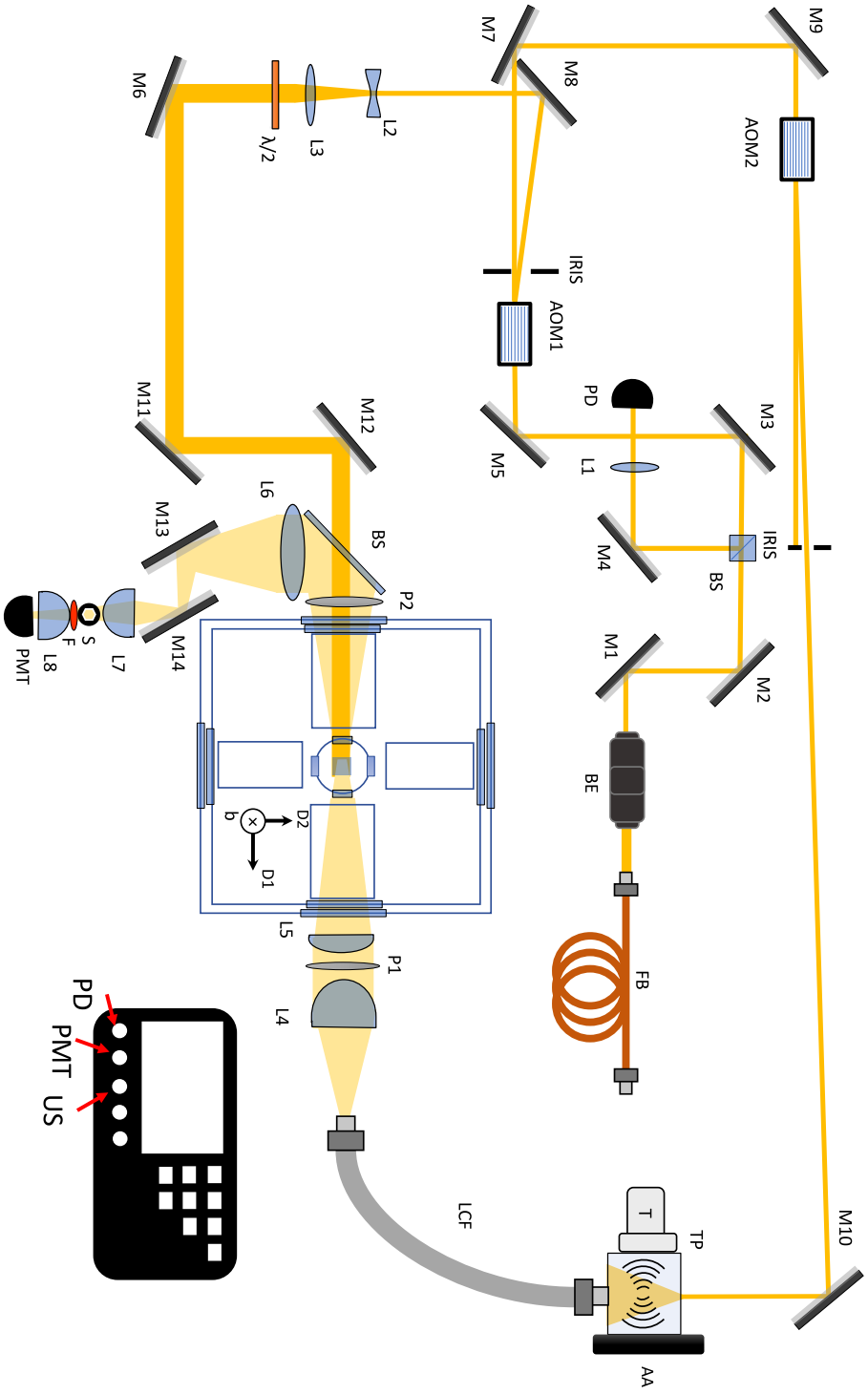

FIGURE 3.8: UOT experiment setup schematic. FB: polarization maintaining single mode fiber; BE: beam expender; M1-M14:mirror; BS:beam splitter; L1-8: lens; PD: photodiode; AOM1-2: acousto-optic modulator; $\lambda/2$: half-wave plate; LCF: liquid core fiber; AA: acoustic absorber; TP: tissue phantom; T:ultrasound transducer; S: shutter; F: fluorescence filter; PMT: photomultiplier tube.

fill the cryostat inner window aperture. The pump beam polarization direction was turned to D_2 by a half-wave plate, then half of its power was cut down by a non-polarizing 50:50 beam splitter. The pump beam went through a linear polarizer P2 (polarization direction: D_2) before it entered the Pr (0.05%):YSO crystal inside the cryostat.

When the first AOM was off, most light ($\approx 80\%$) went to the 0th order. The beam then reached the second AOM (Isomet, 1205c-1). An iris was used to block the 0th order of beam from the second AOM, the 1st order of beam ($\approx 70\%$) sent directly onto the tissue phantom, and the scattered light was collected by a liquid core fiber (Rofin, D = 10 mm, NA = 0.59). A plano-convex L4 (D = 72 mm, f = 52 mm, NA = 0.57) was used to collimate as much diffused light as possible. The collimated beam went through a linear polarizer P1 (only light with polarization direction D_2 can pass through the polarizer) (colorPol VISIR, D = 50.8 mm) then refocused onto the cryostat inner window with another plano-convex lens L5 (D = 50 mm, f = 150 mm, NA = 0.16). Based on the COMSOL ray trace simulation, maximum 8% of the light out of the LCF can be imaged onto the crystal aperture, see Appendix A.2. The spectrally filtered light exiting from the crystal was also diffused light, half amount of the exited polarized light from the BS was then focused by a plano-convex lens L6 (D = 50 mm, f = 150 mm, NA = 0.16). Due to the aperture of the optical shutter S (Uniblitz VS14, D = 14 mm) was small, a pair of aspherical lenses L7 (D = 50 mm, f = 25 mm) and L8 (D = 50 mm, f = 45 mm) were used to focus the beam small on passing through the shutter aperture. The beam was then refocused onto the photo-multiplier tube (Hamamatsu, R943-02) after it went through a 10 nm bandpass filter (Chroma HQ605/10).

The pumping and probing beam paths are counter-propagated to minimize the possibility of accidentally exposing the full power pumping light onto the PMT. The optical shutter was kept closed during pumping and erasing mode, and then it opened for 10 ms to receive the probe signal, afterward, it was closed again. Room light was turned off during the UOT measurement. A black box was also built around PMT to block background and scattered light in the room. The polarizer P2 was used to purify the incoming pumping light polarization and prevent the unpolarized outgoing probing light.

3.3.2 Procedures

From the US measurement, the US has a center frequency of 1.6 MHz and a bandwidth approximately 1 MHz. The prepared spectral filter has bandwidth 1 MHz to cover the US modulated sideband bandwidth. Some aquasonic US gel was applied on the surface of the tissue phantom (air acoustic impedance, 430 $\mathrm{kgm^{-2}\,s^{-1}}$, is a lot different to water, 1.48 $\cdot 10^6$ $\mathrm{kgm^{-2}\,s^{-1}}$ [21]), the gel is used to fix the interface problem so most US would transmit into the agar phantom instead of being reflected

back. The transducer X5-1 was placed in contact with the tissue phantom. If the tissue phantom height and length and width is smaller than 15 cm, the phantom outline shape can be observed in the B mode scan (as echoes). The US scanner was set to PW-mode with the smallest focus, the output trigger of US scanner was then triggering the laser sequence.

Pulse sequence

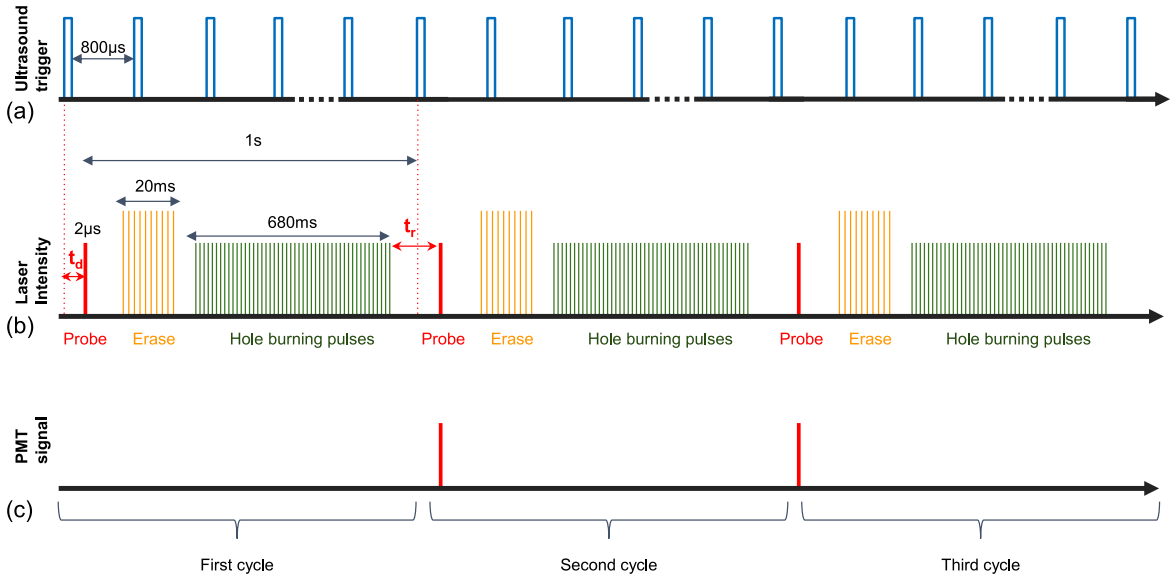

FIGURE 3.9: The experimental pulses sequence. (a) The US output trigger, which is also used to trigger the entire laser sequence. Each US trigger length is 10 μs and the pulse period is 800 μs. (b) Laser pulse sequence. The incoming US trigger triggers the laser sequence, and the first probe pulse will come after certain delay t_d time. The probe pulse has a super-Gaussian shape (the intensity profile is flat over a majority of the area), the pulse length is 20 μs and the pulse FWHM is 2 μs. Due to the spectral filter is not prepared yet, there is no signal readout in the PMT, see sub-figure (c). After 300 erasing pulses, 2000 burning pulses are used to burn the spectral hole. The entire laser sequence duration is around 1 s. The first PMT readout signal can be observed in the second cycle of the pulse sequence. The time t_r between the end of the burning sequence to the first readout is 200 ms+ t_d (waiting time+delay time). The illustration figure is not in scale.

The detailed pulse sequence is presented in figure 3.9. The output trigger from the US triggers the laser pulse sequence after a certain delay time t_d. The delay time is the amount of time required for the US transducer to respond to the trigger plus the traveling time for the pulsed US to reach the desired depth. The laser frequency was shifted to 1.6 MHz, so the US tagged light was centered in the transmission passband of the spectral filter, while the carrier frequency was located outside the spectral window. The experiment was operated in darkness, and the crystal was cooled to 2.17 K. One measurement cycle takes roughly 1 s.

Chapter 4

Results and discussion

4.1 Tissue models

A direct approach of modeling tissue optical properties is by mixing absorber and scatterer with appropriate proportions, such that the tissue phantom optical parameters can be predicted from the individual characteristics. Liquid phantoms allow quick and easy variation of the optical properties and free movement of the detector within the medium, while solid phantom allows manufacturing macroscopic inhomogeneous phantom to simulate biological tissue with complex structure.

4.1.1 Liquid phantom

Intralipid: scattering coefficient

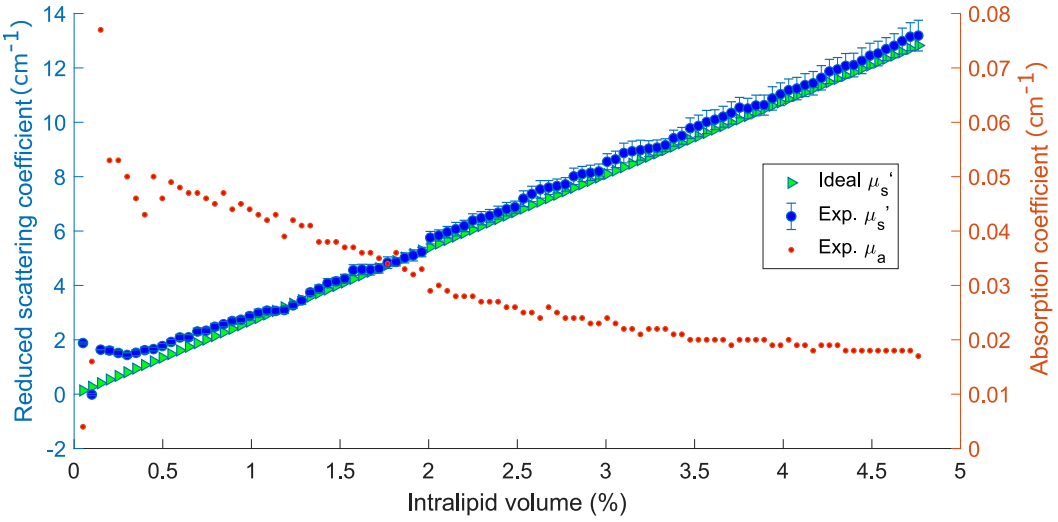

FIGURE 4.1: The effect of the intralipid concentration on μ_s' and $\mu_a$in liquid suspension.

Intralipid phantoms were prepared by using distilled water to dilute the stock intralipid 20% solutions to the concentration of intralipid from 0.05% to 4.75%. During the PTOF measurement, the source and collection fiber separation, d, was kept

constant (20 mm). The d value was also involved during the Monte Carlo fitting progress. If the input d value is larger than the actual separation distance, the photons are expected to travel a longer path, the time dispersion curve FWHM will be broader, curve peak value drops and its position shifts to the later photons side, this would result the μ_s' from the Monte Carlo fitting is larger than the actual value. Thus, for $d\pm$ 0.5 mm, results in a roughly 5% uncertainty in the calculated μ_s'.

The μ_s' increases proportionately to intralipid concentration for both theoretical and experimental data. The theoretical values were calculated by using equation 2.3 at wavelength 606 nm. First few experimental data points for μ_s' are offset from the curve trend, see figure 4.1. This is due to at low scattering coefficient, a large number of photons were reflected from the bottom of the liquid suspension, which causes a computational error for the time of flight. Ideally, intralipid should have no absorption (absorption due to water, μ_a = 0.0026 cm^{-1} at 606 nm[16]), but based on the experimental measurement, the intralipid has 0.02 cm^{-1} absorption coefficient. From figure 4.1, it seems the absorption curve is slowly reaching a plateau with increasing intralipid concentration. It is mostly due to the Monte Carlo fitting. When the scattering is high, less reflected light from the container surface would affect the time dispersion curve fitting result.

Ink: absorption coefficient

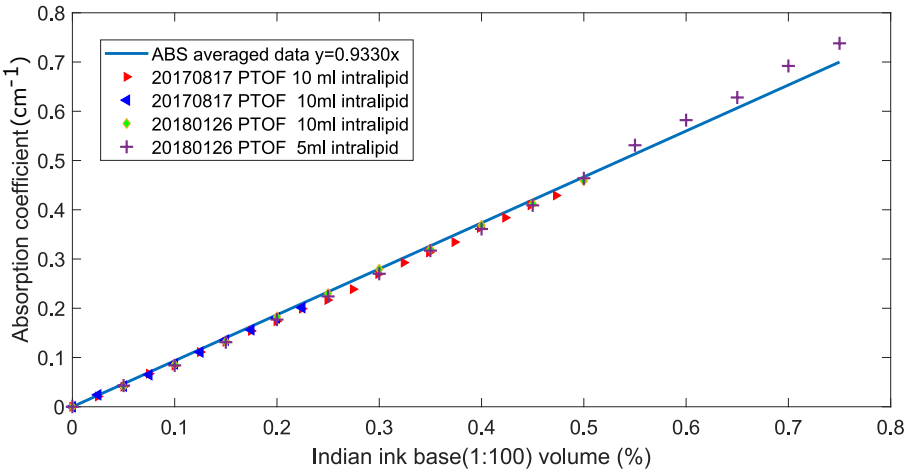

FIGURE 4.2: Absorption coefficient measured vs the Indian ink concentration. Ink was added to intralipid suspension (390 mL distilled water and 10 mL intralipid).

The absorption coefficient is expected to increase proportionately to ink concentration. The manufactured ink base properties were also measured by absorption spectroscopy setup by Di M.Q., her experiment result suggests a linear relationship between μ_a and ink content, y [cm^{-1}] = 0.933 x [%] [15].

For intralipid, the anisotropy of the scatterer suspension is independent of scatterer concentration. However, this does not apply to the ink sample case. First, intralipid particles are on the scale of a nanometer while ink particles are on the scale of a micrometer. Increase large size particle concentration would increase the albedo of the liquid phantom. When the ink base concentration is lower than 0.5%, the trend of the curve is mostly linear, after 0.5% the gradient of curve increases. This could be due to the large size ink particle at high concentration is highly influencing the liquid phantom anisotropy, and the particles could be coalesced and formed larger particles. Another possibility could be there were an insufficient number of photons for Monte Carlo to address an accurate data fitting, as the measurement had to stop at 0.75% since there was not enough signal.

4.1.2 Agar gel phantom

Highly purified agar powder was used to produce solid phantoms, it has approximately no absorption and relatively low scattering. 1% of agar powder is enough to harden the liquid phantom. Since agar powder is often used for standard biological routine experiments, the production conditions are more controlled. Agar phantoms were incorporating intralipid as scatterer and ink as absorber were used in the studies of light propagation in UOT.

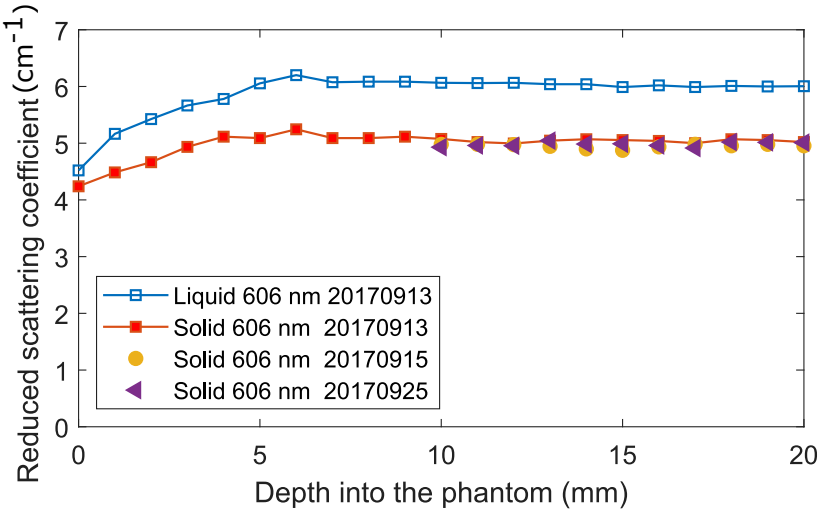

FIGURE 4.3: Repeatability and homogeneity were tested for agar based solid phantoms by looking into the μ_s' variation.

Repeatability and homogeneity are the fundamental requirements of producing a good tissue phantom, along with the ability to characterize its optical properties freely. For a comparison purpose, the homogeneity measurement was also performed on a liquid phantom with the same set of intralipid and ink concentrations, see both figure 4.3 and figure 4.4.

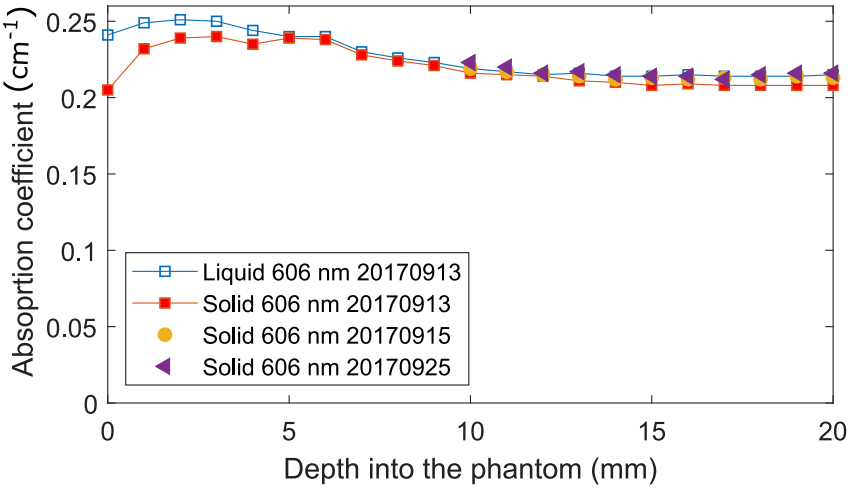

FIGURE 4.4: Repeatability and homogeneity were tested for agar based solid phantom by looking into the μ_a variation

The liquid phantom shown in figure 4.3 and figure 4.4 has a total volume of 400 mL, that includes 10 mL of intralipid and 1 mL of diluted ink base (1:100). The solid phantom has the same total volume and same components compositions before it was solidified. To check the homogeneity of produced agar phantom along the vertical direction, PTOF measurements were performed for 20 different depths with a step size of 1.0 mm. Ideally, at each depth, the PTOF should give out the same μ_s' and μ_a values. However, as both figures shown, the μ_s' and μ_a only reach a constant value when the fibers are at certain depth deep. The first possible explanation is, at shallow depth, there is a strong light reflection from the liquid/solid surface, which causes errors in computational data fitting. In the Monte Carlo, it was assumed that the phantom was infinitely large such that there is no reflection from any surface. For the case of a solid phantom, another possible explanation for the curve trend is due to the production procedure of agar phantom involves temperature changes, there could be pH changes or scatterer aggregation, resulting in a change of the optical properties. It was also observed when the fibers were at shallow depth, there were few small cracks on the agar phantom around the fiber, which would strongly affect the light propagation. When the fiber depth is deeper than 10 mm, both μ_s' and μ_a become constant, μ_s' has 1% variation and μ_a has 2% variation. Another two agar phantoms with the same optical properties were made, and their homogeneity was tested by the same method at different day (from depth 10 mm to 20 mm). The measurement results show very good repeatability of the agar phantom, μ_s' has 4% variation and μ_a has 3% variation among three phantoms.

It was observed from figure 4.3, the reduced scattering coefficient of the agar phantoms has a 16% reduction as compared to the liquid phantom at 606 nm. Author

Beck, G. C. et al. [22] also reported they observed a 30% reduced scattering coefficient reduction when they added 2% agar powder into their liquid phantom. Thus, it could be assumed that the μ_s' reduction dependent on the amount of gelling agent. This effect could be the temperature changes during manufacturing of solid phantom causes the scatterers structure changes. However, overall the μ_s' of the agar phantom is linear with the intralipid concentration, see figure 4.5, therefore by considering the systematic μ_s' reduction due to the gelling agent, it is possible to produce an agar-based phantom with controlled properties.

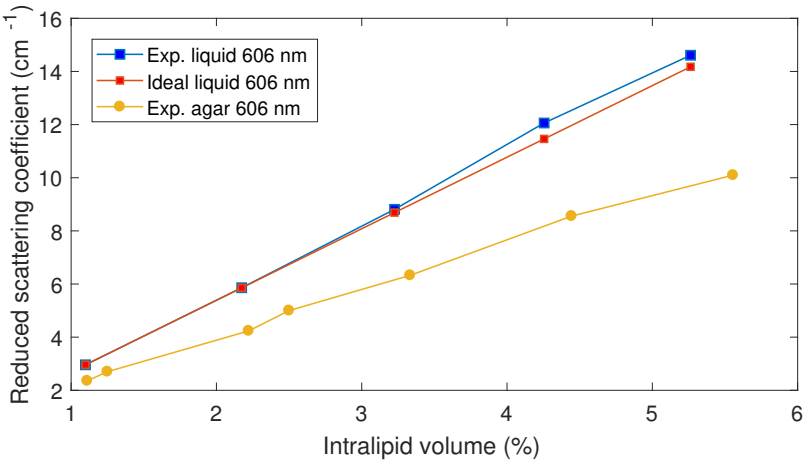

FIGURE 4.5: Adding gelling agent to intralipid-based phantom cause a reduction in the μ_s', but the agar phantom μ_s' is still a linear relation to the intralipid concentration.

4.2 Ultrasound focus

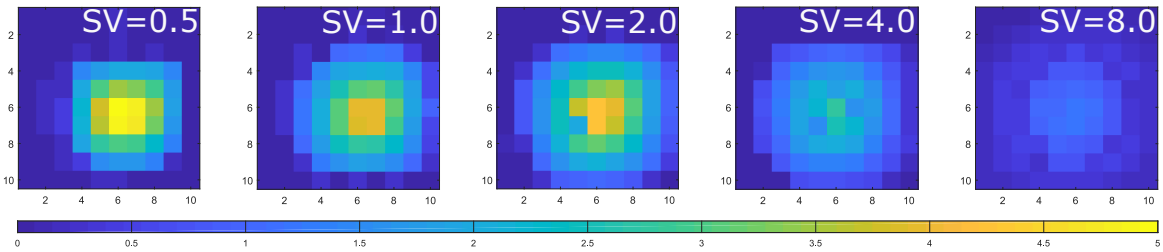

FIGURE 4.6: Profile plots were measured in x and z directions for US focus at different SV setting.

On the US scanner, the US focus size can be changed by SV (sample volume) setting, but the actual focus size (pressure distribution) cannot be observed visually. Thus, the US focus was placed on the tip of the needle hydrophone in the water tank. US focus profiles (10 mm x 10 mm, step size of 1 mm) were measured for five different

SV settings, see figure 4.6. As excepted, when the SV setting value is the smallest, the US forms the relatively smallest US focus, around 2 mm in diameter. For each point of measurement from the profile plot, a corresponding US pulse waveform can be observed. An example of US pulse waveform and its FFT spectrum from the maximum pressure position are shown in figure 4.7, the amplitude read out from oscilloscope was in unit mW, then the program converts the data into Pascal. The width of the pulse spectrum is measured regarding the -3 dB bandwidth, it gives 0.9 MHz bandwidth, and the fundamental frequency is 1.6 MHz.

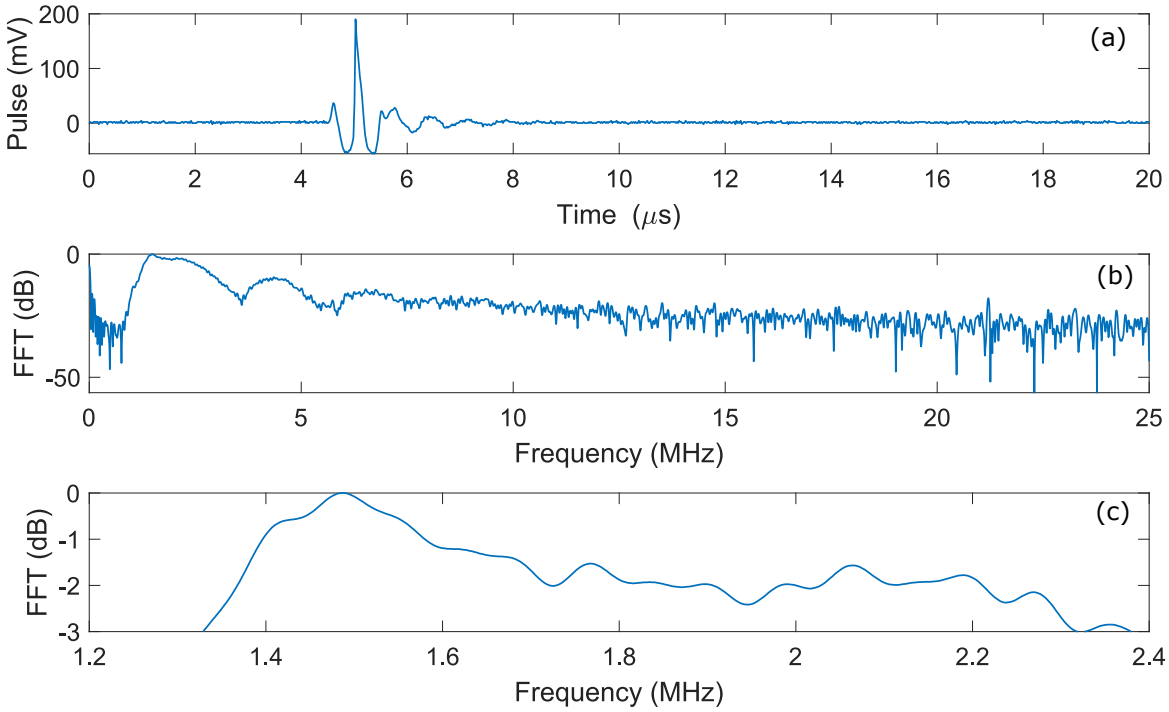

FIGURE 4.7: The US pulse waveform (a) at focus and the corresponding FFT (b) from the positions with maximum pressure. (c) is the zoomed in FFT spectrum to show the bandwidth at -3 dB.

The propagation of the sound wave inside a medium is mainly determined by the medium properties, and it is common to assume the amplitude of the wave at the source is proportional to the amplitude inside the medium. However, when the pressure amplitude is high (> 1 MPa), the velocity of the local particles inside the medium would affect the propagation speed of sound wave inside. When the medium is compressed by high pressure amplitudes, the speed of the sound wave in the compressed region is increased, the phase speed is also increased as the local particle velocity is in the direction of wave propagation direction[21]. Conversely, in the low-pressure region, the particle motion is in the opposite direction to the wave motion, the phase speed is reduced. The rapid changes in the pulse waveform appears as the high-frequency components in the FFT spectrum, the first peak is the fundamental frequency f_0 of the US, the second peak is the second harmonic $2f_0$

and the third peak is the third harmonics $3f_0$ and so on, see FFT spectrum in figure 4.7. The higher the frequency is, the faster US pulse attenuates inside the medium, the power of the US also decreases as it propagates deeper, the pulse shape becomes rounded.

The US focus size determines the lateral resolution of UOT in the transverse direction, the area with higher spatial amplitude distribution has about 2 mm diameter for the smallest US focus setting (see figure 4.6). Thus, 2 mm is the minimum distance that can be imaged for two objects that side to side and perpendicular to the US propagation axis. The limitation of US focus is due to lack of access towards the operating software. Otherwise, the smaller the US focus is in the transverse plane, the better the UOT can resolve small structure and close objects.

Moving the US focus numerically in the transverse plane can perform a lateral 2D imaging. To be able to image in the longitudinal direction, it is necessary to know the axial resolution of UOT: the axial US focus size. The US focus size in axial is depended on the US pulse length, shorter the pulse the higher the resolution. From figure 4.7, the entire pulse length is 3 μs, but for the region with the most rapid amplitude change the pulse length is 1 μs. The US wave propagation speed inside water is about 1.5 mm/μs, in this case, the spatial resolution in the longitudinal direction is in between 1.5 mm to 4.5 mm. The US focus was then placed at a fixed depth, and the US pressure distribution over a volume was measured, see figure 4.8. It can be observed the highest-pressure amplitude is located at where the focus is. However, within $\pm$ 10 mm range, the US lateral resolution was almost the same ($\approx$ 3 mm). This is due to how the phased transducer forms the focus, and this region is usually called the US focal zone. The smallest US lateral focus size changed from 2 mm to 3 mm from figure 4.6 to figure 4.8, this is mostly depended on how good the alignment

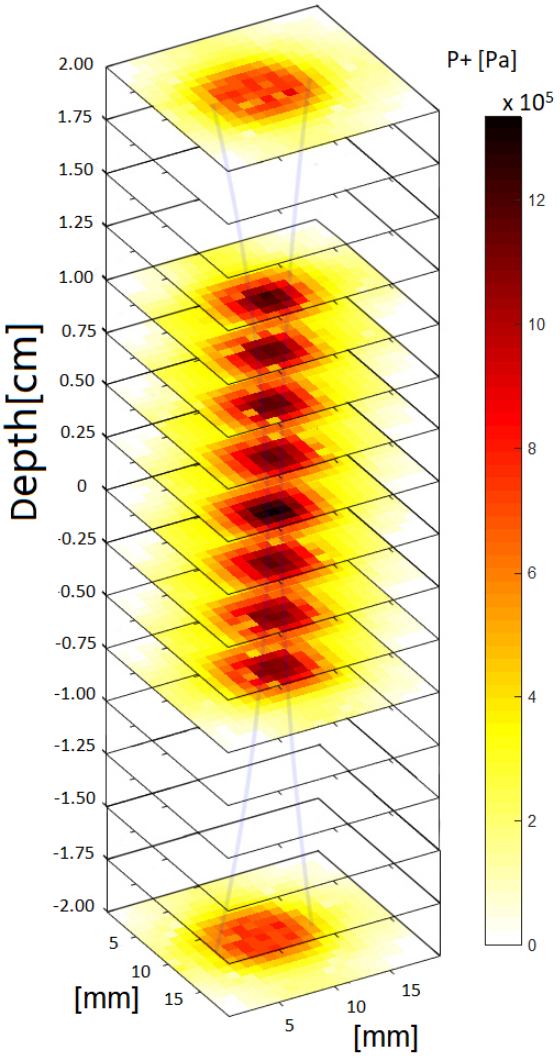

FIGURE 4.8: US focus volume (axial resolution).

was, in figure 4.6 the highest-pressure point is not centered, it is possible the hydrophone was not properly aligned with the US propagation axis. The lateral focus size is larger than the axial focus size, as the lateral focus is dependent on how good the transducer forms the focus while axial focus size is depended on the US pulse length.

4.3 UOT

The UOT experiment was first started with acquiring tagged-photon signal for a single spot (1D), then it was extended to a continuous line (1D) measurement. Agar phantom dimensions are defined by three primary axes that are pair-wise perpendicular (x, y, z), where x is the light propagation direction, y is the US propagation direction.

4.3.1 Tagged ballistic light

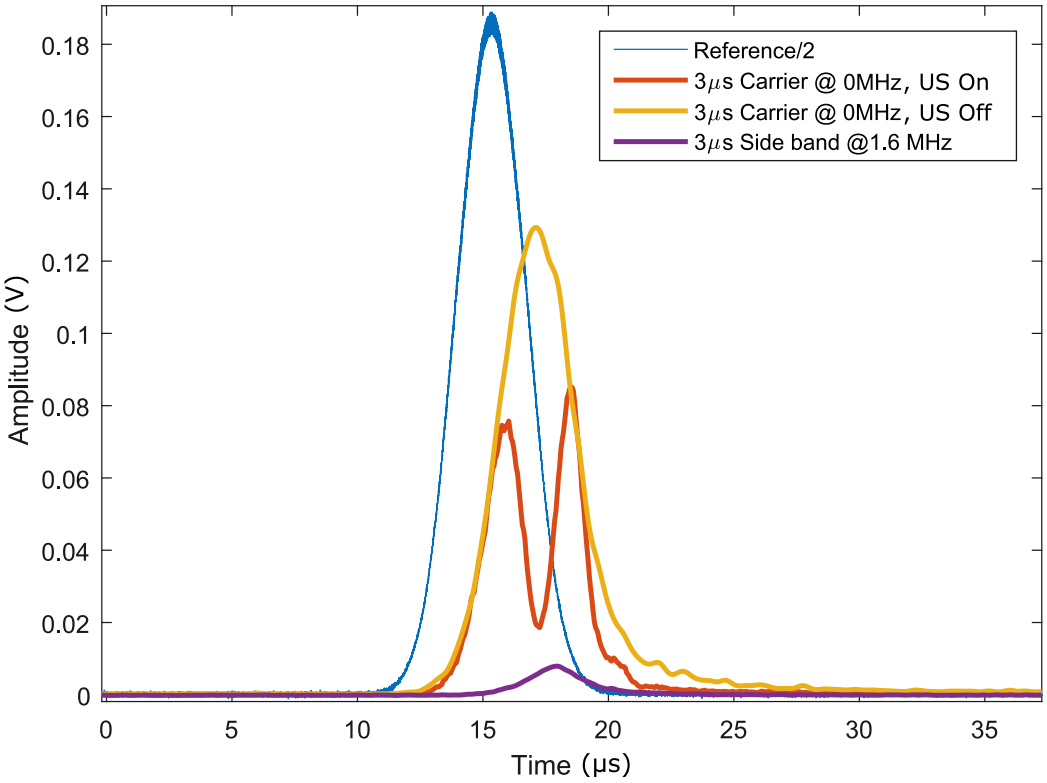

FIGURE 4.9: The ballistic light was tagged by the US pulse. About one-third amount of carrier photons were tagged and diffracted into different orders. The diffraction efficiency of US for the first order at 1.6 MHz was 5%. The PMT cathode to anode voltage was 2000 V, which corresponds to a 6×10^6 gain.

1 D acousto-optic signal was first investigated on a low scattering agar phantom ($\mu_s' = 0.5$ cm^{-1},$\mu_a = 0.02$ cm^{-1}, 20 mm x 50 mm x 50 mm along the x, y and z axes). Due to low scattering property, most lights traveled straight through the phantom. The light collected by the LCF (liquid core fiber) were mainly ballistic and snake photons. The light inside the phantom was tagged directly by the US. In the frequency window, the carrier signal located at 0 MHz and the first US modulated sideband signal located at $\pm$ 1.6 MHz. The light pulse had an FWHM of 3 μs, and the incoming US pulse was roughly 3 μs long as well. All measured acousto-optic signals were averaged 100 times and presented in figure 4.9.

The probe laser center frequency was first set to 0 MHz, and the carrier signal was in the center of the filter transmission window, where all the sideband signals were blocked. The yellow curve in the figure 4.9 showed the carrier signal profile when there was no US, and the red curve shows the carrier profile changes when the US was on. The US was able to tag away one-third of the photons from the carrier. All light went through the spectral filter would experience a 2 μs delay due to slow light effect. The laser center frequency was then shifted to 1.6 MHz. Carrier signal was attenuated entirely (as can be observed from the figure, there is no leakage from the carrier), and the sideband signal (tagged photons) is presented in figure 4.9 with a purple curve. The area under each curve corresponds to the number of photons. By comparing the area under the sideband and carrier curves, 5% photons from the carrier were tagged and diffracted into the first sideband. When the laser

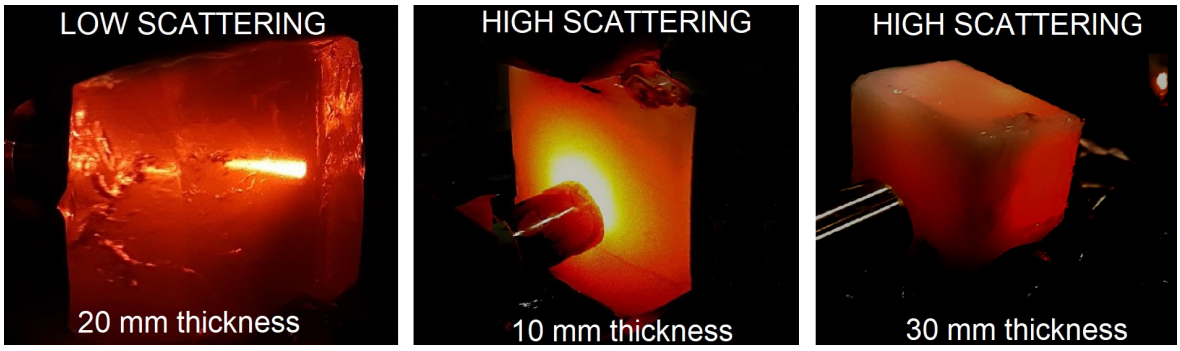

FIGURE 4.10: For a thin and low scattering phantom, most light traveled inside remain their original propagation directions. For a thick and high scattering phantom, photons undergo more multiple scattering events, light escaped the phantom in all directions.

frequency was set to 0 MHz and the US was on, a pit appeared in the center of the carrier signal profile. The cutoff area from the carrier profile corresponds to the number of photons tagged away by the US. During the procedure of timing the US and laser pulse, it was observed that if the timing was off by 1 μs (the smallest step size), the sideband signal was still detectable except its position shifted in the time domain. A detail explanation is presented in Appendix A.3, the main reason for such a phenomenon is due to the incoming laser pulse length is too long. The US signal had an average pulse length of 3 μs, but the active range that generates

a strong acousto-optic interaction signal was less than 3 μs (see figure 4.7). This problem was fixed by shorting the laser pulse length to 2 μs.

4.3.2 Tagged scattered light

The advantage of tagging ballistic light is not only able to achieve a strong acousto-optic interaction but also easy to position the US focus. If the laser was in CW mode, the beam positioning inside the phantom was visible. However, such phantom optical properties are not comparable to the realistic tissue. Multiple scattering events and strong absorption inside the tissue cause the light information to be lost. The acousto-optic interaction of high scattering medium was then investigated.

1.8 cm thick phantom

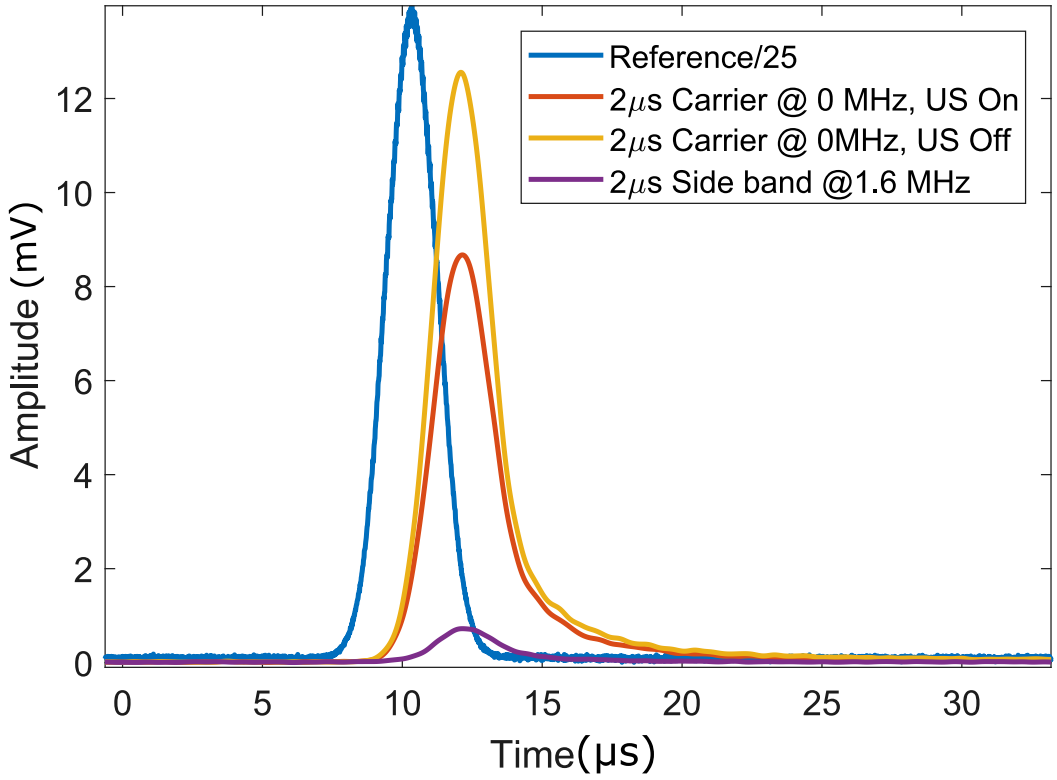

FIGURE 4.11: Light traveled through an 18 mm thick highly scattering phantom, diffused light at a single spot was tagged by the US. 2000 V high voltage was applied to the PMT, which corresponds to a 6×10^6 gain.

An 18 mm x 50 mm x 50 mm (along x, y and z axes) highly scattering agar phantom was used ($\mu_s' = 5$ cm $^{-1}$, $\mu_a = 0.02$ cm $^{-1}$). When the laser was in the continuous-wave (CW) mode, it was observed that the light scattered and excited from all surfaces of the phantom, but most light (snake photons) still remembered their initial beam

path after diffusion. Light undergoes scattering in 3 different phantoms is presented in figure 4.10. When the thickness of the highly scattering phantom increases, light experiences a larger number of scattering events, more photons are absorbed, and fewer snake photons remain. Instead, more light is diffused into all directions. A 2 μs light pulse was used. Figure 4.11 shows the tagged and untagged carrier signals. The way to position the spectral filter was the same as described in subsection 4.3.1. If the laser center frequency was set to 0 MHz, all sideband signals were attenuated, and carrier signal was transmitted. If the laser center frequency was set to 1.6 MHz, the carrier signal was attenuated, and the tagged photon signal was transmitted.

Compared to the case of ballistic light, fewer photons were modulated by the US: the light was more spread away in the highly scattering phantom, fewer photons were concentrated in the acousto-optic interaction region. Signals were averaged 100 times, and all signals that went through the spectral filter experienced a 2 μs delay. The diffracted efficiency into the first positive order was calculated, it remains 5%.

4.0 cm thick phantom

A 40 mm x 50 mm x 50 mm (along x, y and z axes) highly scattering phantom was used (μ_s' = 5 cm $^{-1}$, μ_a = 0.02 cm $^{-1}$). The tagged photon signal was very weak, as shown in figure 4.12. Thus, during this measurement, a 10 mT magnetic field was applied to the crystal to extend the lifetime of the spectral filter. The initial idea was to extend the spectral filter lifetime and sent in multiple probe pulses to accumulate the signal. According to Di M.Q.[15], applying an external magnetic field had a minor effect on the filter suppression, but the filter edge became less sharp. However, in the end, the accumulation did not work. The pulse sequence was kept the same; one probe pulse was used per cycle.

As the thickness of the phantom was increased, the number of tagged photons was expected to decrease while the diffraction efficiency of the US should be the same. Each group of signals was averaged for 100 times and plotted in figure 4.12. Both carrier and sideband signals experienced a 2 μs delay. When the laser center frequency was set to 1.6 MHz and the tagged photons signal transmitted through the spectral filter, there was some untagged light leakage. Those leaked photons did not experience a time delay from the slow light effect, which means they did not enter the transmission window of the spectral filter. Thus, it can be confirmed that they were the leakage from the pump beam path due to reflection or scattering in the optical components. The photon leakage from the pump beam can be avoided by adding an extra mechanical shutter in the pump beam path. Back to the displayed tagged photon signal in figure 4.12, its profile looks like the background (untagged) photons and the tagged (with 2 μs delay) photons merged. The untagged light background was not recorded during the measurement, but it was confirmed that it originated from the pump beam. Thus, the untagged background light should be a factor

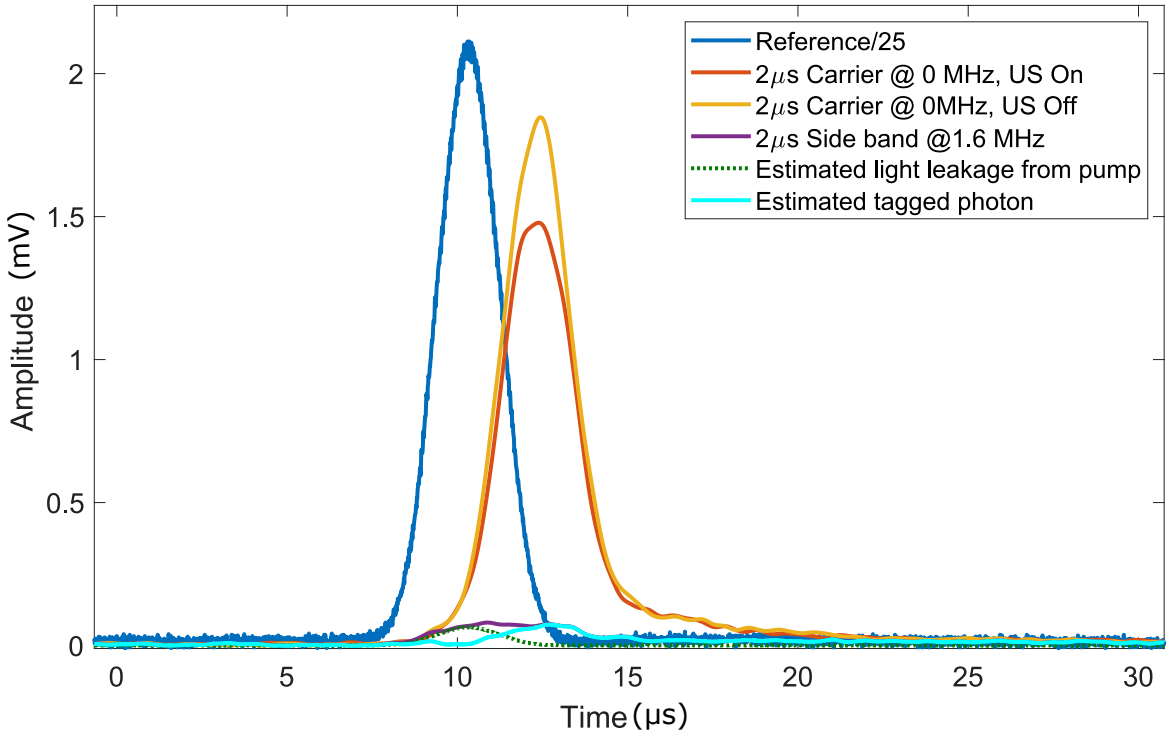

FIGURE 4.12: A 40 mm thick phantom was used. Photons are more diffused thus the tagged photons signal was expected to decrease.

k of the reference signal. The k value can be obtained by first finding the (x,y) coordinates of the reference signal maxima, then read out the y value for the merged signal at the same x coordinate, the ratio between two y values is the k factor ($k = 0.0304$). The estimated untagged light noise is also plotted in figure 4.12 with a green dash line. By subtracting the estimated pump light leakage from the measured sideband signal would give the estimated tagged photons signal. The diffraction efficiency was calculated by dividing the area of the estimated tagged-photon signal to the area of the carrier without the US, and it is 6.64% for this measurement. The increase in the diffraction efficiency could be due to the spectral filter profile changed when 10 mT magnetic field was applied, few photons from the carrier leaked in, or the leakage could always have been there, but it was never a problem when the detected signal was relatively stronger. The probe light intensity was 15 mW during this measurement, 40 mm thickness was the limit with the current UOT setup.

1D line measurement

A single spot acousto-optic signal was proven to be detectable. Thus, moving the US focus along a line and readout the sideband signal would give a 1D line measurement. In an ideal situation, the US focus is moved to different depths in y-axis step by step by adjusting the relative phase of the individual US transducer elements, and the probe pulse time delay is varied to compensate the US propagation

time. The US propagation speed is about 1.5 mm/μs inside the agar phantom, the step-size of time delay is 1 μs. In the US focus measurement, it showed that for a continuous US beam, the US focus shape is more like a thin hourglass rather than a sphere, see figure 4.8. Within a $\pm$ 10 mm range, the pressure distribution difference was minor, the pressure at the center of the 'hourglass' (where the US focus located) was 1.3 MPa, where the center pressure 10 mm away from the focus along the y-axis was 1.1 MPa. The US pulses formed a relatively strong focus before it reached the desired focus region. Thus, to perform a quick 1D line measurement, the US focus was fixed at the desired location, then the laser pulses were timed so it would interact with the US pulse before, at, or after the focus within the focus zone. The advantage of this method is the US focus does not need to be numerically moved in the US scanner, a 1D line measurement in the US propagation direction can be performed just by varying the probe pulse delay time. For example, if the US focus was at the depth d, a perfect timing between US pulses and laser pulses would be t_d, if now the delay time was changed to t_d - 1 μs, the US pulses would interact with light 1.5 mm above the focus zone, acousto-optic signal came from depth d + 1.5 mm. vice versa, if the delay time was t_d + 1 μs, the readout acousto-optic signal came from depth d - 1.5 mm.

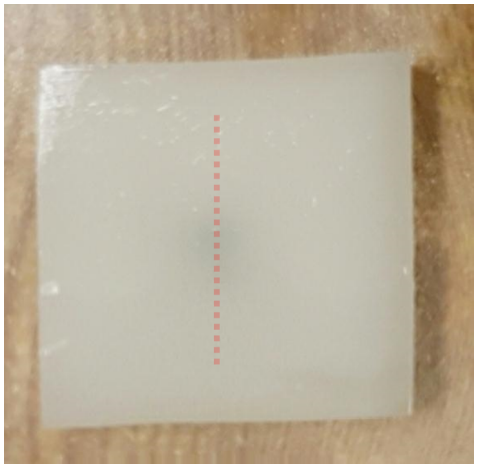

FIGURE 4.13: A 10 mm thick highly scattering phantom with an absorber planted inside, the geometry of the absorber is hardly observable due to multi-scattering. The red dash line indicates the US scanning line, in total 21 points were scanned.

A 10 mm x 50 mm x 50 mm highly scattering agar phantom (μ_s' = 5 cm $^{-1}$, μ_a = 0.02 cm $^{-1}$) was first used to perform a blank sample 1D line measurement. The probe light was hitting the center of the phantom, and the US pulses scanned in the center line with a step size of 1.5 mm (1 μs). The detected acousto-optic signals distribution along the scanning line is corresponding to the light irradiance within the phantom, see figure 4.14. Then a second agar phantom with the same dimensions and optical properties was used, but in the center of this phantom, there was an

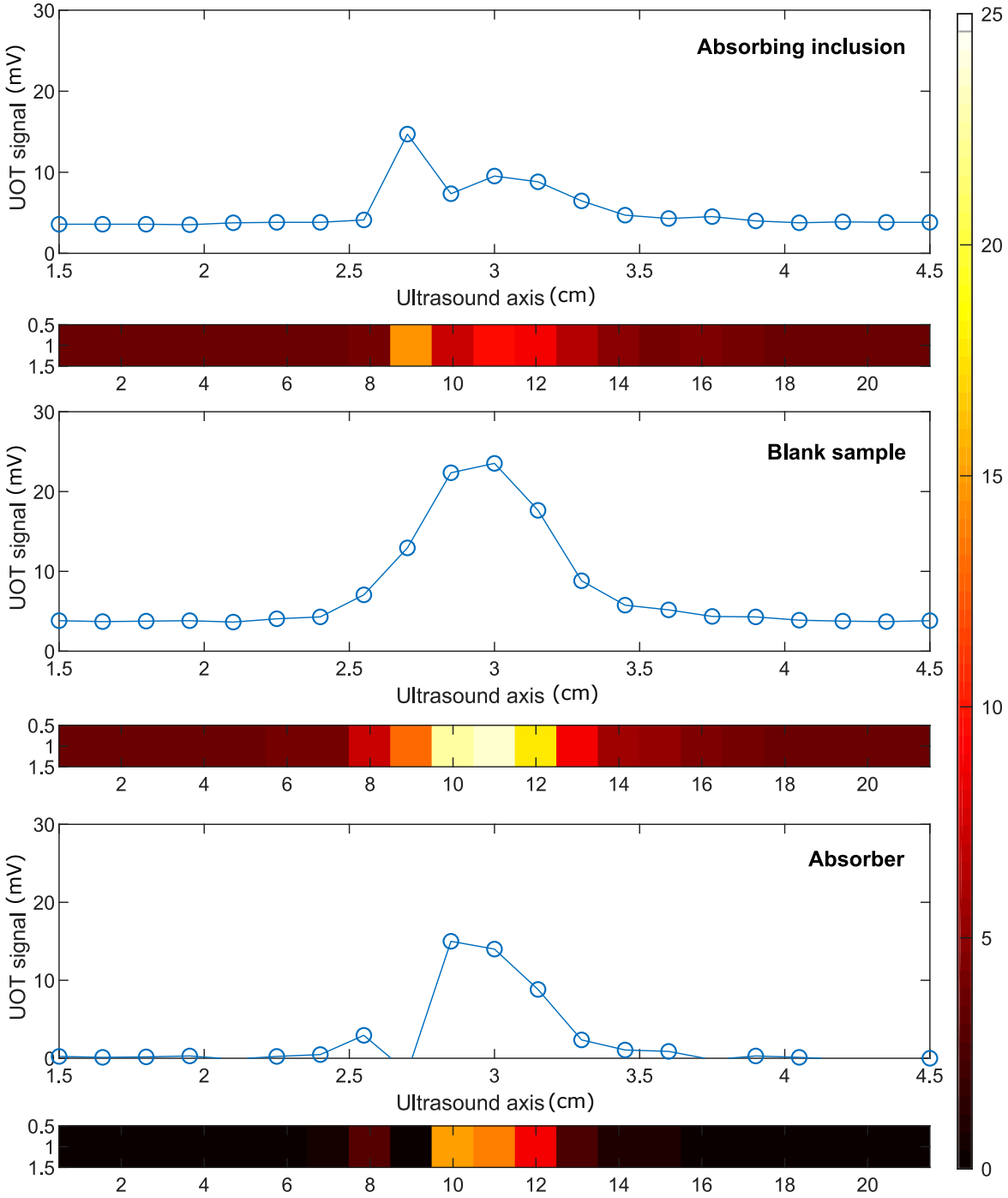

FIGURE 4.14: 1D line measurement was performed on a highly scattering agar phantom with a localized absorber inside. Absorber dimensions were 5 mm x 5 mm x 5 mm. The 1D line measurement was perform in the y axis. The blank sample signal minus absorbing inclusion signal gives the absorber position and dimensions.

absorber implanted. The size of the absorber was 5 mm x 5 mm x 5 mm. A photo of the phantom with the absorbing inclusion is shown in figure 4.13. The reason for choosing this size of absorber was, the current UOT resolution was around 2 - 3 mm, if the absorber was too small, it may not be observed in the line scanning; if the absorber was too big, it would absorb a large proportion of light scattered inside the medium, it will lower the acousto-optic signal strength when there was already very low amount of probe light. The reason for choosing a thin slice of scattering phantom was, the goal was to perform deep tissue imaging with UOT, but before it was possible to move forward towards a higher depth, it was necessary to prove the system was able to perform tissue imaging based on the acousto-optic signals. With a 10 mm thickness, the localization of the absorber in the highly scattering phantom can be observed by eyes. Thus, the UOT imaged result can be used to compare with the visual observation.

The 1D line measurement result of absorbing inclusion phantom is presented in figure 4.14, the probe light was hitting the center of the phantom (also hitting the absorber), US pulses scanned in the center line of the phantom. By subtracting the blank sample and absorber inclusion sample signals, it gives the absorber signal distribution in the 1D line. The absorber dimension according to the UOT signal was roughly 4*1.5 mm, that was 6 mm while the real size was 5 mm. Thus, the current UOT setup can perform interior scanning of a highly scattering medium based on the acousto-optic signals, but its resolution is highly limited by the US focus size, and the penetration depth is limited by the probe light power.

Chapter 5

Conclusion and Outlook

5.1 Conclusion

In summary, this thesis work encompassed manufacture tissue models with controlled optical properties and homogeneity, study the ultrasound property and development of ultrasound optical tomography (UOT) system. Strong absorption and scattering properties of the tissue are the primary factors that were limiting the optically-based imaging system development. Use a wavelength from the optical window with low tissue absorption would increase the light penetration depth, but it cannot fix the optical information loss due to multi-scattering events. The principle of UOT is to tag the photons in the region of interest with ultrasound and then filter the tagged photons with a high finesse spectral filter. The UOT system was very sensitive to laser intensity and stability. When there was only 30 nJ (15 mW$\times$2 μs) probe light, the current UOT system can detect acousto-optic interaction signal for a 40 mm thick highly scattering phantom, and it was able to perform a 1D line measurement for a highly scattering phantom (μ_s' = 5 cm^{-1}) with an inclusion in the center, the inclusion dimension can be estimated from the 1D line measurement. The laser safety level is 20 mJ/cm ^{2} for pulsed light [23]. Thus, the laser energy used in this thesis work has an improvement factor of $\approx 10^6$. Although the relation between the penetration depth in a highly scattering medium and the laser power is nonlinear, increasing the probe laser power would still improve the penetration depth and contrast-to-noise ratio.

5.2 Outlook

Lack of control of the ultrasound scanner and low probing laser light power are the two main deficiencies of the current UOT system. The signal strength of UOT is dependent on the light irradiance inside the tissue and the focus size of the ultrasound. In the current system, the UOT spatial resolution is 2 to 3 mm, which is far from the goal of resolving tissue structural properties in μm scale. The resolution of UOT can be improved by using a smaller ultrasound focus, but that does not necessarily mean that the UOT signal would be improved. A smaller ultrasound volume would modulate less number of photons, and the sideband signal might be

so weak that cannot be distinguished from the detector dark noise. More photons can be tagged if the ultrasound has a better diffraction efficiency. The diffraction efficiency of ultrasound can theoretically be improved by increasing the ultrasound pressure level. Overall, the key to enhance UOT system performance is to find the optimal balance between the UOT resolution and signal strength and deliver more photons into the deep tissue and efficiently extract the weak tagged photons signal from the background. Tm:$Y_3Al_5O_{12}$ (Tm $^{+3}$:YAG) crystal has a transition at 793 nm, this wavelength is within the optical window, and it can be used to burn a persistent spectral hole at 1.8 K and last for more than 30 s [24]. This crystal could be a good choice for future developing a UOT system for clinical applications

There are a range of different improvements that can be addressed to the current UOT setup. Since the lifetime of the spectral filter can be extended by applying an external magnetic field, send in multiple probe pulses and accumulate the signals would speed up the UOT data acquiring time (instead of sending one probe pulse per cycle and wait for 100 s for a 100 times data averaging, 100 probe pulses can be sent in one cycle and the averaged data would give the same result). The laser safety level for pulse light was beam size dependent, expanding the probing beam to a bigger size would allow a higher power probe light, bigger volume of tissue would be illuminated.

Appendix A

Supplement

A.1 Cryostat

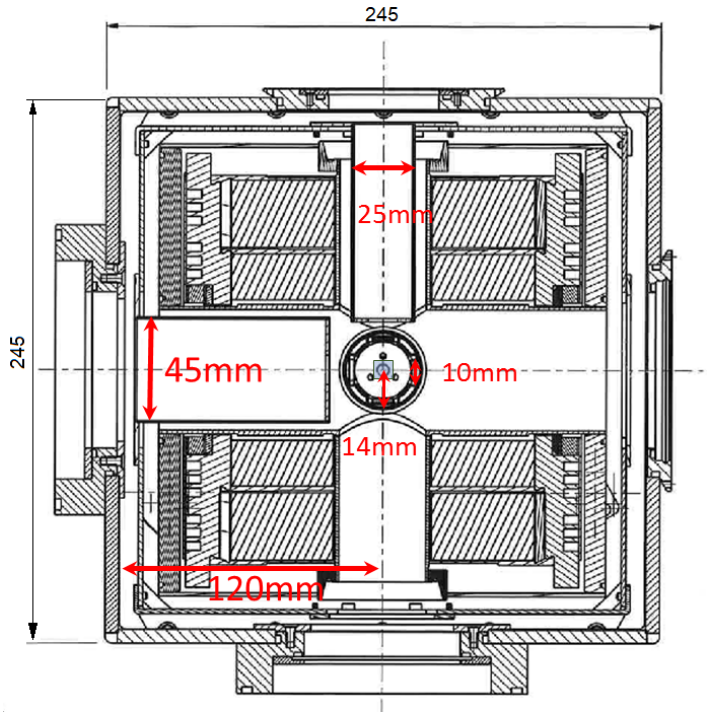

FIGURE A.1: The blueprint of the used cryostat.

Since the UOT probe light mainly consist of diffused light, and it is necessary to be able to gather as much diffuse light as possible into the crystal. The geometry of the cryostat (etendue) determines the arrangement of the experimental setup and incoming light polarization direction. The cryostat has four outer windows, two of them has a diameter of 45 mm, and the other two has 25 mm diameter. The collected diffused light must go into the cryostat through the 45 mm diameter window to maximize the etendue. Close to the center of the cryostat, there are other four inner windows with a diameter of 10 mm. Due to this limitation, the edges of the pumping (burning) beam will be cut into a 10 mm diameter large beam, the 10 mm x 10 mm

x 12 mm crystal will therefore not be pumped entirely. So the probe and pump beamlines must be placed parallel instead of crossed and entering from different sides.

A.2 Light coupling

Comsol Multiphysics 5.3 a was used to perform the ray tracing simulation. The structure of the cryostat was first generated in the simulation, and the main limiting factor is the acceptance angle of the cryostat: the outer window of the crystal has a diameter 45mm, and the inner window has a diameter 10 mm. The light source was a Lambertian emitter with diameter of 10 mm, and it was used to simulate the diffuse light comes out of the liquid core fiber. The liquid core fiber has a numerical aperture of 0.59. Thus, the Lambertian emitter ray direction is conical with a cone angle of $\sin^{-1}(0.59)$. The aspherical lens used to collect the diffuse light has a numerical aperture of 0.57, it can collimate most light from the light source, see figure A.2 for the ray tracing and the schematic of the optical system. Ray termination and blockers were used to cut off light has escaped the optical system to save the computer GPU usage. A detector was placed in front of the source to record the outgoing light intensity, then the detector was placed after the inner window and right before the crystal. From the simulation displayed (see figure A.3), maximum 8% of light managed to reach the crystal.

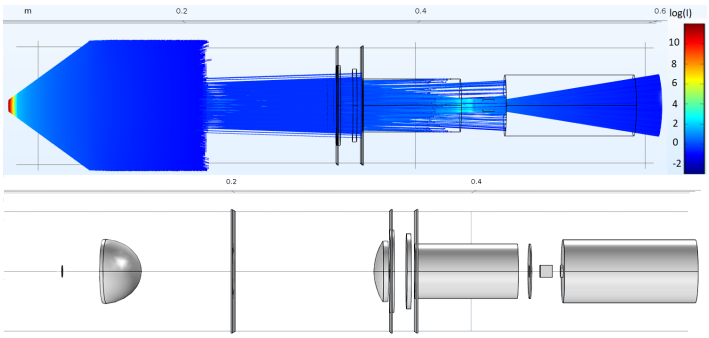

FIGURE A.2: Ray trajectories and optical system component schematic.

A.3 UOT resolution issue

The resolution of UOT is depended on the focus size of the US. From the US measurement (see figure 4.6 and figure 4.8), the smallest US focus dimensions in the light propagation direction was 2 - 3 mm and 3 μs (4.5 mm) in the US propagation direction. However, as shown in figure 4.7, the effective region where the US tags most photons are smaller than 3 μs. So, when the US pulse interacts with a 3 μs long laser pulse, US cannot tag sufficient number of photons even the pulses timing

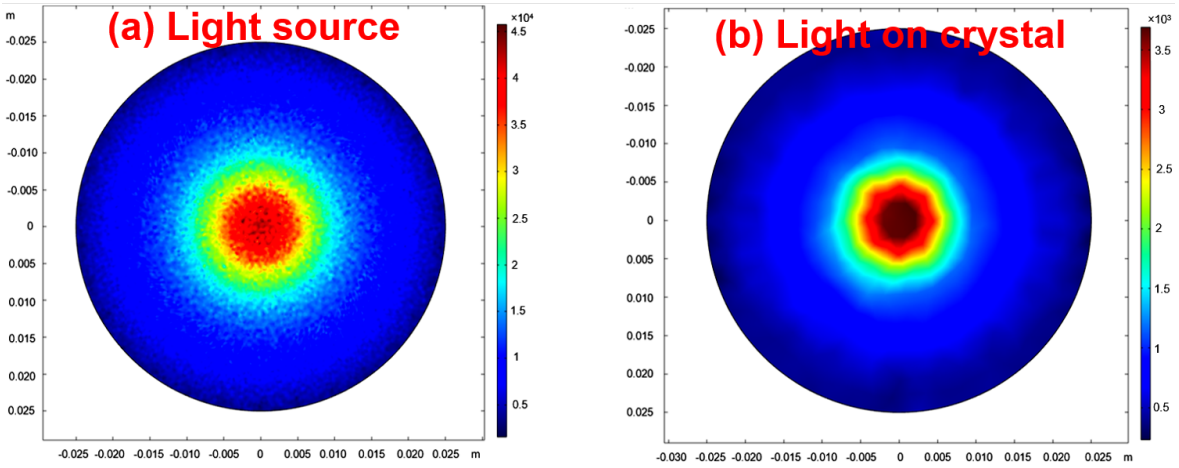

FIGURE A.3: Light intensity distribution from the source output and the input before it enters the crystal. Due to the cut off from the inner window, the focused diffuse light could not cover the 10 mm x 10 mm surface area of the crystal.

was correct. As shown in figure A.4, the sideband signal was detectable when the timing was 1 μs off, its position was shifted based on where the light and US interacted. This problem was fixed by shorting the pulse length to 2 μs, and the sideband signal becomes only detectable when the acoustic and laser pulses interaction was perfectly timed.

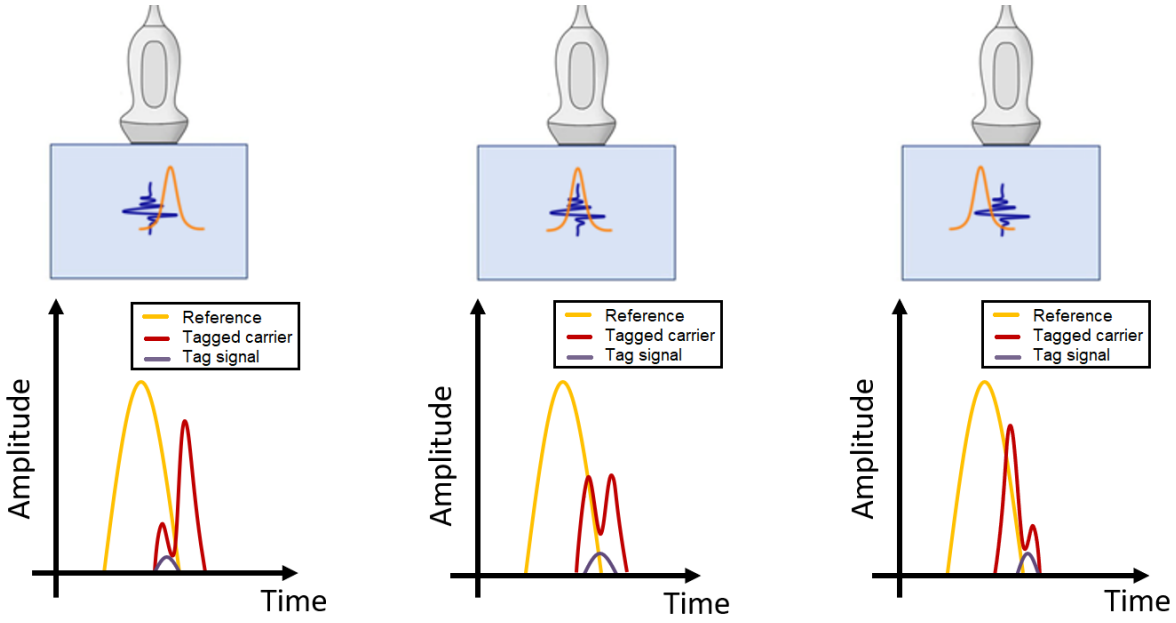

FIGURE A.4: Ballistic photons were tagged by the US in a low scattering sample. However, due to the laser pulse length is too long, there was still signal readout even the timing between pulses was wrong. The resolution of UOT is depended on the size of US focus. The speed of US inside agar was roughly 1.5 mm/μs, and an ideal acousto-optic interaction would be both the laser and US pulse have the same length.

Bibliography

[1] H. Liu, "Advancing Upconversion Emissions for Biomedical Imaging", *PhD thesis, LRAP-484, Department of Atomic Physics, Lund University*, 2014.

[2] J. M. Menter, "Temperature dependence of collagen fluorescence", eng, *Photochemical & Photobiological Sciences: Official Journal of the European Photochemistry Association and the European Society for Photobiology*, vol. 5, no. 4, pp. 403–410, Apr. 2006.

[3] A. Walther, L. Rippe, L. V. Wang, S. Andersson-Engels, and S. Kröll, "Analysis of the potential for non-invasive imaging of oxygenation at heart depth, using ultrasound optical tomography (UOT) or photo-acoustic tomography (PAT)", EN, *Biomedical Optics Express*, vol. 8, no. 10, pp. 4523–4536, Oct. 2017.

[4] T. Valery, "Light scattering study of tissues", vol. 40, p. 495, Oct. 2007.

[5] T. Valery, "Tissue optics and photonics: Light-tissue interaction", *Journal of Biomedical Photonics & Engineering*, vol. 1, no. 2, 2015.

[6] P. Di Ninni, F. Martelli, and G. Zaccanti, "Intralipid: Towards a diffusive reference standard for optical", vol. 56, N21–8, Jan. 2011.

[7] R. Michels, F. Foschum, and A. Kienle, "Optical properties of fat emulsions", *Opt. Express*, vol. 16, no. 8, pp. 5907–5925, Apr. 2008.

[8] M. J. C. V. Gemert, S. L. Jacques, H. J. C. M. Sterenborg, and W. M. Star, "Skin optics", *IEEE Transactions on Biomedical Engineering*, vol. 36, no. 12, pp. 1146–1154, Dec. 1989.

[9] C. Boudoux, *Fundamentals of biomedical optics: From light interactions with cells to complex imaging systems*. Pollux, 2017.

[10] E. Alerstam, S. Andersson-Engels, and T. Svensson, "White monte carlo for time-resolved photon migration", *Journal of Biomedical Optics*, vol. 13, 2008.

[11] A. Kienle and M. S. Patterson, "Determination of the optical properties of turbid media from a single monte carlo simulation", *Physics in Medicine and Biology*, vol. 41, no. 10, p. 2221, 1996.

[12] E. Alerstam, S. Andersson-Engels, and T. Svensson, "Parallel computing with graphics processing units for high-speed monte carlo simulation of photon migration", *Journal of Biomedical Optics*, vol. 13, 2008.

[13] E. Alerstam, S. Andersson-Engels, and T. Svensson, "Improved accuracy in time-resolved diffuse reflectance spectroscopy", *Opt. Express*, vol. 16, no. 14, Jul. 2008.

[14] W. Lihong V., "Mechanisms of ultrasonic modulation of multiply scattered coherent light: An analytic model", *Phys. Rev. Lett.*, vol. 87, p. 043 903, 4 Jul. 2001.

[15] M. Q. Di, "Preparation of materials for deep tissue imaging with slow light", *MSc thesis, LRAP-545, Department of Atomic Physics, Lund University*, 2018.

[16] V. M. Zolotarev, B. A. Mikhilov, L. L. Alperovich, and S. I. Popov, "Dispersion and absorption of liquid water in the infrared and radio regions of the spectrum", *Optics and Spectroscopy*, vol. 27, pp. 430–432, 1969.

[17] I. Driver, J. W. Feather, P. R. King, and J. B. Dawson, "The optical properties of aqueous suspensions of intralipid, a fat emulsion", *Physics in Medicine & Biology*, vol. 34, no. 12, p. 1927, 1989.

[18] K. Pal, A. K. Banthia, and D. K. Majumdar, "Polymeric hydrogels: Characterization and biomedical applications", *Designed Monomers and Polymers*, vol. 12, no. 3, pp. 197–220, 2009.

[19] R. Cubeddu, A. Pifferi, P. Taroni, A. Torricelli, and G. Valentini, "A solid tissue phantom for photon migration studies", *Physics in Medicine & Biology*, vol. 42, no. 10, p. 1971, 1997.

[20] B. Julsgaard, A. Walther, S. Kröll, and L. Rippe, "Understanding laser stabilization using spectral hole burning", *Opt. Express*, vol. 15, no. 18, pp. 11 444–11 465, Sep. 2007.

[21] A. T. Peter R. Hoskins Kevin Martin, *Diagnostic ultrasound: Physics and equipment*. Cambridge University Press, 2010.

[22] G. C. Beck, N. Akgün, A. Rück, and R. Steiner, "Design and Characterisation of a Tissue Phantom System for Optical Diagnostics", *Lasers in Medical Science*, vol. 13, pp. 160–171, Oct. 1998.

[23] *American national standard for the safe use of lasers, standard z136.1- 2000 (ansi, inc., new york, 2000).*

[24] N. Ohlsson, M. Nilsson, S. Kröll, and R. K. Mohan, "Long-time-storage mechanism for tm:yag in a magnetic field", *Opt. Lett.*, vol. 28, no. 6, pp. 450–452, Mar. 2003.